Theoretical Investigation of Intersystem Crossing in the Cyanonitrene Molecule, ^{1}NCN → ^{3}NCN

Mark Pfeifle,* Yuri Georgievskii, Ahren W. Jasper, Stephen J. Klippenstein

Chemical Sciences and Engineering Division, Argonne National Laboratory, Argonne, Illinois 60439, USA

To be published in JOURNAL OF CHEMICAL PHYSICS

Correspondence to: Mark Pfeifle; e-mail: mpfeifle@anl.gov

ABSTRACT:

The NCN diradical is an important intermediate of prompt nitric oxide formation in flames. The mechanism of intersystem crossing (ISC) in the NCN molecule formed via pyrolysis or photolysis of NCN_3 is of relevance to the interpretation of experiments that utilize NCN_3 as a precursor for laboratory studies of NCN kinetics. This mechanism has been investigated by means of multi-reference configuration interaction (MRCI) calculations. From the potential energy surfaces for NCN_3 dissociation, it was inferred that both thermal and photo-chemical decomposition initially lead to NCN in its lowest singlet state, $\tilde{a}\ ^1\Delta_g$, with a possible contribution from the $\tilde{b}\ ^1\Sigma_g^+$ state at low photolysis wavelengths. Direct formation of the triplet ground state $\tilde{X}\ ^3\Sigma_g^-$ is also feasible for the photolytic pathway. An analysis of surface crossings between $\tilde{a}$ or $\tilde{b}$ and the triplet ground state $\tilde{X}\ ^3\Sigma_g^-$ in the absence and presence of a helium atom revealed an ISC channel ^{1}NCN ($\tilde{a}$) $\rightarrow$ ^{3}NCN ($\tilde{X}$) via a strongly bent structure. However, its barrier of 38 kcal mol^{-1} relative to the singlet minimum turned out to be much too high to explain the fast ISC observed in experiments. A rigid-bender model including Renner-Teller interactions was used to examine the occurrence of mixed-multiplicity rovibrational states—so-called gateway states—that could enhance collision-induced ISC. The results of this study indicate that a gateway mechanism is probably not operative in the case of the $\tilde{a}/\tilde{X}$ pair of states in NCN.

I. INTRODUCTION

In recent years, the cyanonitrene radical (NCN) has received significant attention after it had been identified as an important intermediate in the nitric oxide (NO) formation mechanism in combustion.[1,2] For decades, the key step of prompt-NO formation[3] in fuel-rich regions of flames was believed to be the spin-forbidden reaction $^2CH + {}^1N_2 \rightarrow {}^1HCN + {}^4N$.[4] However, the occurrence of severe discrepancies between experiments and *ab initio* rate calculations[5] led to the discovery by Lin and co-workers of the spin-allowed pathway $^2CH + {}^1N_2 \rightarrow {}^2H + {}^3NCN$.[6,7] This channel was subsequently confirmed by shock-tube experiments[8] and high-level theoretical kinetics calculations.[9] NCN was further directly detected in flames by means of laser-induced fluorescence (LIF).[10,11] Owing to its relevance in combustion chemistry, numerous experimental and computational studies on the kinetics of NCN reactions have been carried out in recent years[12-16] (for a more comprehensive selection, see e.g. Ref. 17).

The NCN molecule itself had already been discovered in the 1960s by Jennings and Linnett[18] via ultraviolet (UV) emission and unambiguously identified by Herzberg and Travis[19] by analyzing the corresponding absorption spectrum. Further UV,[20-25] infrared absorption,[26-28] LIF,[25,29] laser magnetic resonance[30,31] and photoelectron spectroscopy[32,33] studies afforded deeper insight into the molecular and electronic structure of NCN. A compilation of the available spectroscopic data can be found in the review by Jacox.[34] NCN has been the focus of several theoretical works as well. Early Hartree-Fock[35,36] and density functional theory studies[37] were followed by various multi-reference analyses. Martin et al.[38] utilized the complete active space self-consistent field (CASSCF) method in combination with coupled-cluster calculations to predict the structure and vibrational frequencies of ground-state NCN. Suter et al.[39] investigated the hyperfine coupling in NCN and related molecules with multi-reference configuration interaction (MRCI) theory. The excited electronic states of NCN were the main emphasis of the works by Perić et al.[40,41] (MRCI) and Rajendra and Chandra[42] (CASSCF, MRCI and complete active space second order perturbation theory, CASPT2). Thermochemical properties were addressed in studies by Clifford et al.[32] (CBS model chemistries[43]) and Canneaux et al.[44] (CBS and G3/G4[45] model chemistries).

A convenient NCN precursor for spectroscopic and kinetic studies is cyanogen azide (NCN_3):

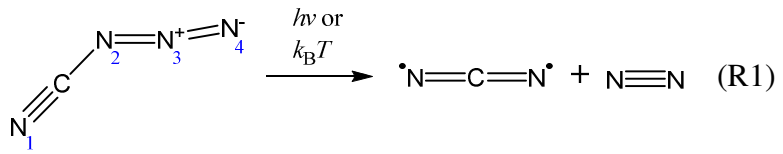

The potential of NCN_3 as a photolytic NCN source was discovered by Milligan et al.,[46] and a recent computational study by Ci et al.[47] gives first indications about the underlying photo-dissociation pathways. The thermal decomposition of gas-phase NCN_3 was first described by Marsh and Hermes,[48] who characterized the NCN dimer as a final product. Benard et al.[49] used gaseous NCN_3 in combination with active nitrogen to synthesize solid carbon nitride (C_3N_4) films and proposed NCN from NCN_3 pyrolysis as a probable gas-phase intermediate for the film growth process. Under appropriate experimental conditions, the first-generation product NCN is available for kinetic studies, as demonstrated by Busch et al.[14] (see also Ref. 50) and by Dammeier et al.[17,51] in shock-tube studies.

For such kinetics experiments, the timescale of ^{3}NCN production—both in pyrolysis and photolysis setups—is critical. As NCN is most likely formed in a singlet state initially (see, e.g., Refs. 47 and 49), intersystem crossing (ISC) must occur in order to observe the desired triplet ground state. This potentially delays ^{3}NCN formation, which can in turn complicate the interpretation of kinetic measurements. Detailed information on the relaxation kinetics allows one to choose the experimental conditions to minimize the impact of undesired induction periods or ^{1}NCN + X side reactions in competition with the ^{3}NCN + X reaction of interest.

In their first NCN_3 decomposition study, Dammeier et al.[17] carried out shock-tube experiments between 546 and 1257 K at total particle densities of 2-4 × 10^{18} molecules cm^{-3} of argon bath gas. NCN in its triplet ground state ($\tilde{X}\ ^3\Sigma_g^-$) was detected by time-resolved laser absorption at 329 nm. The resulting ^{3}NCN concentration-time profiles were fit by an offset exponential function. Due to the temperature and pressure dependence of the first-order rate coefficients obtained in this way, the rate determining step was attributed to unimolecular NCN_3 decomposition for $T < 700$ K and to collision-induced ISC (CIISC), ^{1}NCN + M → ^{3}NCN + M, for $T > 700$ K. An activation energy of ca. 5 kcal mol^{-1} was determined for the presumed CIISC step. Master equation calculations for the dissociation reaction were carried out to support this interpretation. The time offset in the rise of the ^{3}NCN signals was ascribed to either experimental artifacts of the shock-tube technique or relaxation processes within NCN. In an extended investigation from the same group,[51] thermal

(shock-tube) as well as photolytic (193 nm, room-temperature slow-flow cell) NCN_3 decomposition was used to generate NCN. In addition to the triplet ground state, ^{1}NCN ($\tilde{a}\ ^1\Delta_g$) was detected via absorption at 333 nm. In both the high-temperature and room-temperature setups, transient ^{1}NCN signals were observed within the first few hundred μs of the reaction. Consumption rates of ^{1}NCN were found to agree reasonably well with ^{3}NCN formation rates at the same conditions. Bi-exponential fits were used to extract elementary rate coefficients as a function of temperature and pressure from the concentration-time profiles. The authors concluded that in both setups CIISC is the rate-determining step that governs ^{1}NCN consumption and delayed ^{3}NCN formation, except for the shock-tube experiments below 700 K where unimolecular NCN_3 decomposition is rate-determining.

Very recently, a systematic LIF flow-cell study of NCN collisional relaxation was performed by Hetzler and Olzmann[52] for P = 10-800 mbar, T = 240-293 K with He, Ne, Ar, Kr, H_2, N_2, O_2 and N_2O as bath gases. NCN_3 was photo-dissociated at 248 nm, thus depositing a considerably smaller amount of energy into the molecule in comparison with the photolysis study in Ref. 51. ^{3}NCN concentrations were monitored by resonant LIF (329 nm), while fluorescence of ^{1}NCN could not be observed, presumably due to radiation-less relaxation. A delayed (~0.1-60 μs) ^{3}NCN signal increase was found, which could be fitted with offset bi-exponential functions where both time constants describe a signal increase. The resulting first-order rate constants k_{fast} (and k_{slow}) in the range 10^4-10^7 s^{-1} (10^3-10^6 s^{-1}) were proportional to the collider gas particle density, yielding second-order quenching rate coefficients k'_{fast} (k'_{slow}) in the range 7-80 (1-10) × 10^{-14} cm^3 $molecule^{-1}$ s^{-1} at room temperature, depending on the bath gas. The data for argon (T = 293 K) can be compared with those of Ref. 51: good agreement is found for k_{fast}, while k_{slow} from Ref. 52 is larger than in Ref. 51 and exhibits a linear pressure-dependence over the entire pressure range. The dependence of k'_{fast} and k'_{slow} on bath gas (for the noble gases) and temperature was interpreted in terms of the SSH (Schwartz, Slawsky and Herzfeld[53,54]) model for vibration-to-translation (V-T) energy transfer. At the same time, evidence for vibration-to-vibration (V-V) enhancement for the polyatomic bath gases was found. As a consequence, k_{fast} and k_{slow} were tentatively ascribed to two parallel vibrational relaxation pathways within ^{3}NCN, while a contribution from CIISC to these rate constants was not completely ruled out.

To summarize, the experimental evidence indicates that both thermal and photolytic cleavage of NCN_3 leads to ^{1}NCN initially. The slowest process in the ^{3}NCN formation mechanism seems to take place on a timescale of μs to ms and exhibits pressure dependence as well as weak temperature dependence. This rate-determining step may be identified with CIISC or with vibrational relaxation of ^{3}NCN. In the latter case, intramolecular or collision-induced ISC would be fast enough to be obscured by the slower vibrational quenching. Consistent with either interpretation, the experiments suggest that the ISC step is a fast process with a relatively low barrier that is accessible at temperatures as low as 240 K.

The goal of this study was to shed light on possible ISC pathways and to relate these to the experimental observations. First, the NCN_3 dissociation mechanism was analyzed to obtain information on the initial population of NCN states (section IIIIII.A). Potential energy surfaces (PESs) of the lowest electronic states, based on high-level electronic structure theory, were then calculated to examine potential surface-crossing pathways from ^{1}NCN to ^{3}NCN (section III.B). It was found that these channels involve relatively high barriers on the order of 40 kcal mol^{-1}. Finally, the existence of so-called gateway states—rovibrational states with mixed-multiplicity character—was evaluated based on a rigid-bender molecular model, taking into account the Renner-Teller (RT) vibronic interaction of the participating degenerate $^1\Delta_g$ state (section III.C). The existence of such gateway states could in principle explain fast ISC in the absence of low-energy surface crossings. However, the results of our investigation indicate that a gateway state mechanism is unlikely to be important for NCN.

II. QUANTUM-CHEMICAL METHODS

All quantum-chemical calculations were carried out with the Molpro 2012.1 package.[55] CCSDT(Q)[56] computations were accomplished with the interface to MRCC.[57,58] To determine the heat of formation of NCN_3 and its barrier to thermal dissociation, a composite coupled-cluster scheme was used: Geometries, harmonic vibrational frequencies and zero-point corrections were obtained at the CCSD(T) level with Dunning's aug-cc-pVTZ basis set.[59] Subsequent single-point calculations were carried out using the explicitly correlated CCSD(T)-F12a method[60] with the same basis set. An additive correction term ΔE_{hlc} for higher-level electron correlation was included by computing the difference between CCSDT(Q) and CCSD(T) energies with the cc-pVDZ basis set. The short notation CCF12 will be used in the remainder of the paper to refer to this

combination of methods. Structures and harmonic frequencies for all relevant species are listed in the Supporting Information.

The excited states of NCN were examined with the internally contracted MRCI method with single and double excitations[61-63] and relaxed-reference Davidson corrections[64] for higher order excitations (MR-CISD+Q, in the following abbreviated as MRCI). In general, state-averaged CASSCF references with equal weights for all considered states were used, unless noted otherwise. Spin-orbit matrix elements were calculated at the CASSCF level using the full Breit-Pauli operator. For the NCN_3 dissociation study, calculations at the CASPT2 level[65] were also performed. Here, the internally contracted RS2C variant[66] was chosen, which is computationally economical, especially for large active spaces. In some calculations for NCN_3, the smaller def2-TZVP basis[67] was used instead of aug-cc-pVTZ.

In Fig. 1, the orbitals for the full-valence (14e,12o) active space of NCN are depicted. Some calculations were performed with a reduced (10e,10o) active space. Here, the $2\sigma_u$ and $3\sigma_g$ orbitals, which are nearly doubly occupied in most situations, were moved from the active space into the closed shell. In the reduced (6e,6o) space that was used for potential energy scans, only the $1\pi_u$, $1\pi_g$ and $2\pi_u$ orbitals were included. In the Supplementary Material, this (6e,6o) space is additionally shown for the bent NCN configuration at the minimum of the seam of crossing between ^{1}NCN and ^{3}NCN.

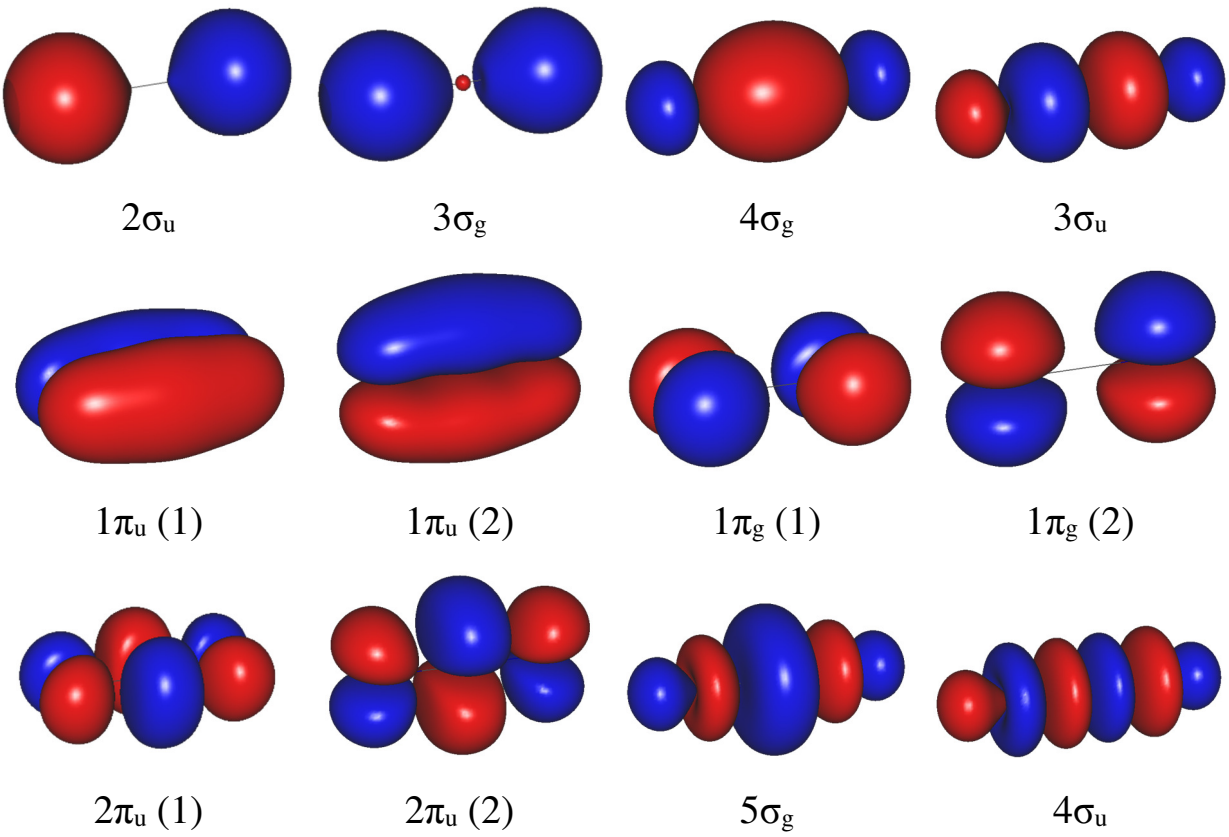

FIG. 1. Orbital visualization for the full-valence (14 electrons, 12 orbitals) active space of NCN, obtained at the CASSCF(14e,12o)/aug-cc-pVTZ level.

The (18e,14o) active space used for the NCN_3 dissociation analysis is illustrated in Fig. 2. With respect to the closed-shell NCN_3 configuration, it includes six occupied orbitals of a′ symmetry, three occupied a″ orbitals and five unoccupied orbitals (three a′, two a″). In the limit of large fragment separation, these correlate with all π orbitals of N_2 and NCN, as well as the $2\sigma_u$, $3\sigma_g$, $4\sigma_g$ and $3\sigma_u$ orbitals of NCN (see also upper row in Fig. 1).

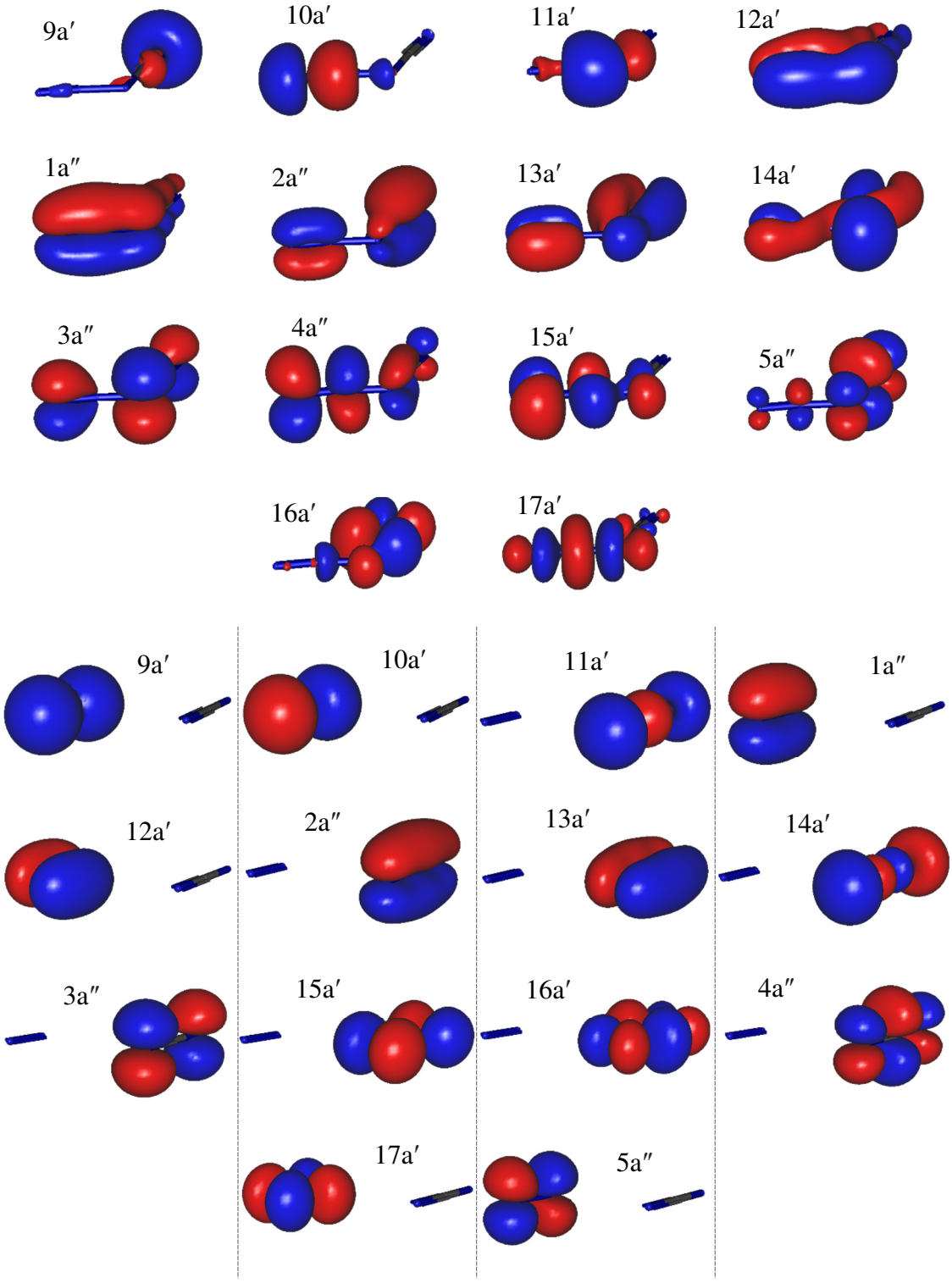

FIG. 2. Orbital visualization for the 18 electron, 14 orbital active space of NCN_3 (top) and the approximately separated fragments N_2 + NCN (bottom, distance between the closest N atoms: 3.0 Å) obtained at the CASSCF(18e,14o)/def2-TZVP level.

As in the case of NCN, a reduced version of this large and expensive active space was also employed. This (10e,10o) active space is shown in Fig. 3. It is obtained by moving four orbitals of a′ symmetry from the active space into the closed shells. As a result, it consists solely of N_2 and NCN π orbitals in the asymptotic limit.

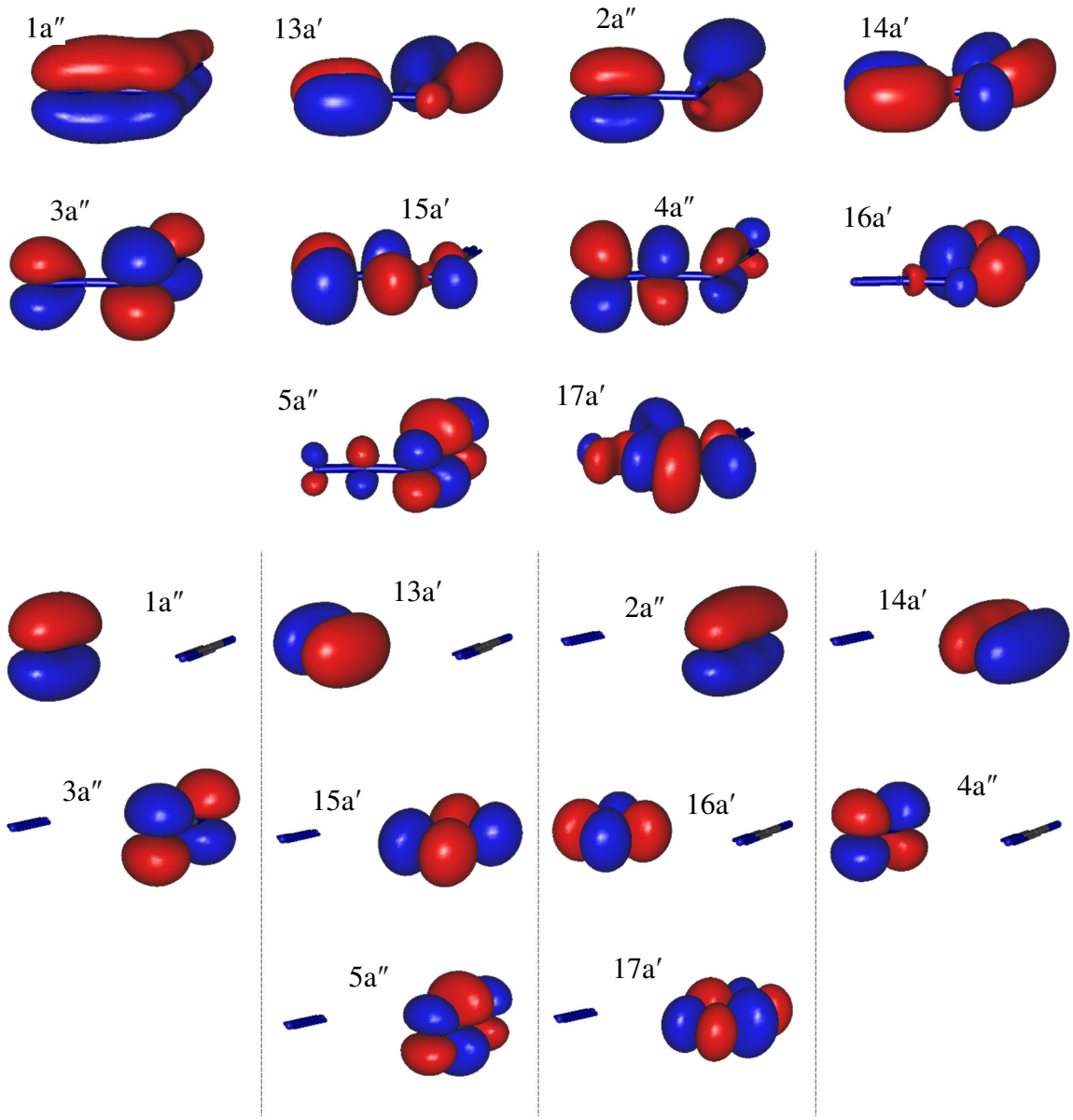

FIG. 3. Orbital visualization for the 10 electron, 10 orbital active space of NCN_3 (top) and the approximately separated fragments N_2 + NCN (bottom, distance between the closest N atoms: 3.0 Å) obtained at the CASSCF(10e,10o)/def2-TZVP level.

III. RESULTS AND DISCUSSION

A. Thermal and Photo-Induced Dissociation of Cyanogen Azide (NCN_3)

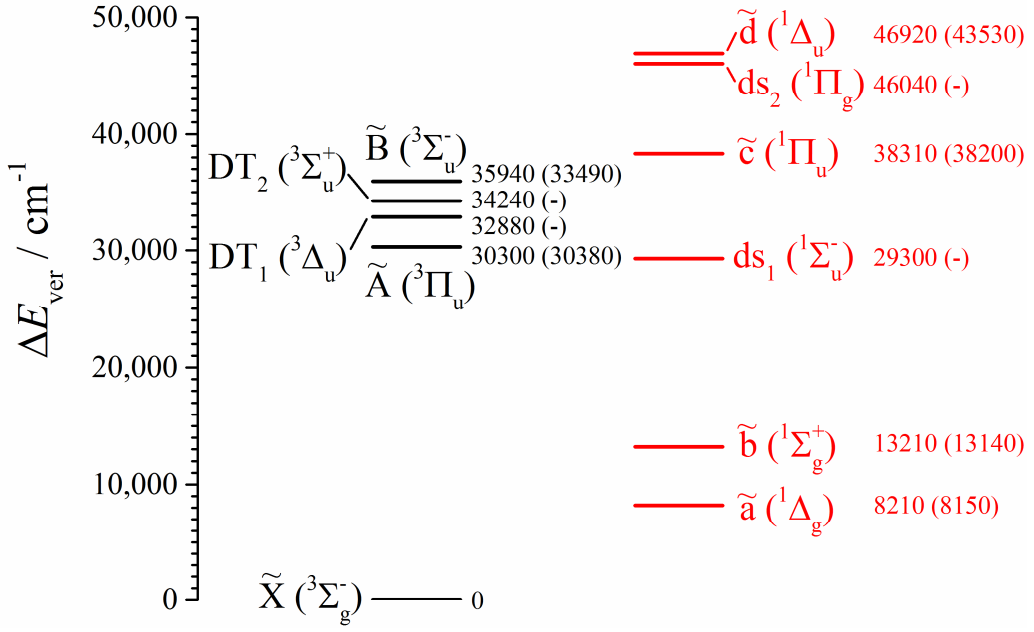

FIG. 4. Calculated vertical excitation energies for the lowest triplet (l.h.s., black) and singlet (r.h.s., red) states of NCN, obtained at the MRCI(14e,12o)/aug-cc-pVTZ level for the linear ground state equilibrium structure (r_{CN} = 1.236 Å). The numbers in parentheses are experimentally determined T_0 term values[34] (differences between vibrational ground states of the electronic states).

In Fig. 4, the energetic order of the lowest five triplet and six singlet states of NCN is depicted. A full-valence active space was used so that states of diverse electronic character were equally well described. All energies were calculated at the optimized ground-state structure (linear, $D_{\infty h}$, r_{CN} = 1.236 Å, optimized with MRCI(14e,12o)/aug-cc-pVTZ without state averaging), i.e. they correspond to vertical excitation energies. The quoted experimental values refer to T_0, the difference between the vibrational ground states of the respective electronic states, and can therefore be compared only qualitatively to the theoretical values. Good agreement is found for most of the spectroscopically detected states, except for the $\tilde{B}$ and $\tilde{d}$ states for which a deviation on the order of 3000 cm^{-1} is observed. The source of this discrepancy is unclear.

The $\tilde{X}$, $\tilde{a}$ and $\tilde{b}$ states are predominantly characterized by a $(4\sigma_g)^2(1\pi_u)^4(3\sigma_u)^2(1\pi_g)^2$ configuration, while the $\tilde{A}$ and $\tilde{c}$ states result from excitation of a σ_u electron into a π_g orbital, yielding $(4\sigma_g)^2(1\pi_u)^4(3\sigma_u)^1(1\pi_g)^3$. Another configuration, $(4\sigma_g)^2(1\pi_u)^3(3\sigma_u)^2(1\pi_g)^3$, gives rise to $\tilde{B}$ and $\tilde{d}$, as

well as three dark states. The dark singlet state—denoted in this work as ds_1 to avoid confusion with existing name schemes—and the dark triplet states DT_1 and DT_2, have not yet been reported in the theoretical or experimental literature to the best of our knowledge. Another dark singlet state ds_2 is best described by a $(4\sigma_g)^1(1\pi_u)^4(3\sigma_u)^2(1\pi_g)^3$ configuration. The lowest states $\tilde{X}$, $\tilde{a}$ and $\tilde{b}$ are of particular interest in this study because they are—as will be demonstrated later—the only states populated under typical NCN_3 dissociation conditions.

Before discussing the correlation of states between NCN_3 and NCN + N_2, it is useful to first consider the energetics of the bond fission process. For the spin-forbidden reaction

$$^1NCN_3 \rightarrow NCN\ (\tilde{X}\ ^3\Sigma_g^-) + N_2\ (\tilde{X}\ ^1\Sigma_g^+), \quad (R2)$$

Ci et al. report a reaction energy, $\Delta_R E$, of –0.8 kcal mol^{-1} at the MRCI+Q//CAS(10e, 9o)/6-311+G(2df) level,[47] where it is not clear if this value contains any zero-point or thermal corrections. The G3 calculations of Dammeier et al. yielded a value of –16.0 kcal mol^{-1} for $\Delta_R H$(0 K),[17] whereas Benard et al. obtained $\Delta_R H$(298 K) = –11.3 kcal mol^{-1} at the B3LYP/6-311+G(2df) level.[49] Given this spread in the literature data, reexamining the thermochemistry of this reaction seems worthwhile.

The heat of formation for NCN($\tilde{X}\ ^3\Sigma_g^-$), $\Delta_f H$ (0 K) = (109.0 ± 0.3) kcal mol^{-1}, can been found in the Active Thermochemical Tables (ATcT);[68,69] for N_2 it is zero by convention. The heat of formation of NCN_3 was calculated in this work via the isodesmic reaction

$$HN_3 + HCN \rightarrow NCN_3 + H_2. \quad (R3)$$

Its reaction enthalpy at 0 K was determined to be +18.3 kcal mol^{-1} at the CCF12 level. Combined with the ATcT heats of formation (+71.3 ± 0.14) and (+30.99 ± 0.02) kcal mol^{-1} for HN_3 and HCN respectively, this yields $\Delta_f H$ (0 K) = 120.6 kcal mol^{-1} for NCN_3. According to this calculated value, (R2) is exothermic by 11.6 kcal mol^{-1}, nearly coinciding with the value from Ref. 49. For the spin-allowed thermal reaction on the singlet surface,

$$^1NCN_3 \rightarrow NCN\ (\tilde{a}\ ^1\Delta_g) + N_2\ (\tilde{X}\ ^1\Sigma_g^+) \quad (R4)$$

cyanonitrene's triplet-singlet splitting of 23.3 kcal mol^{-1} (Ref. 33, see also Fig. 4) has to be taken into account, resulting in $\Delta_R H$ = +11.7 kcal mol^{-1}. The CCF12 barrier for this dissociation is 25.7 kcal mol^{-1}. Due to this potential energy profile, the initial internal energy in thermally generated

NCN (ã $^1\Delta_g$) is expected to be relatively small, particularly since the released energy (14 kcal mol^{-1} + thermal contribution) is partitioned into both fragments as well as their relative translational motion. Therefore, chemical activation for a subsequent reaction of NCN (ã $^1\Delta_g$), such as ISC to NCN ($\tilde{X}$ $^3\Sigma_g^-$), can only be significant if its barrier is on the order of 14 kcal mol^{-1} or lower. However, it will be shown in section III.B that ISC in ^{1}NCN has a significantly larger threshold energy.

As mentioned in the introduction, NCN_3 can also be fragmented photochemically. The main difference relative to thermally activated dissociation is the significantly larger energy available in the system, thus allowing access to more reaction channels. Besides fragmentation to NCN + N_2, a competitive channel producing CN + N_3 also exists.[47,70] With $\Delta_R H(0\ \mathrm{K}) = 91.9\ \mathrm{kcal\ mol^{-1}}$ (where the NCN_3 heat of formation is from this work, and the CN and N_3 heats of formation are from ATcT), this is a potential side reaction at photolysis wavelengths below 310 nm.

To narrow the possible manifold of initially populated NCN electronic states, a correlation diagram along the N-N bond dissociation coordinate was calculated. To this end, constrained single-state geometry optimizations of the lowest singlet state at a series of increasing N_2-N_3 bond distances (see (R1) for the atom numbering) were performed and then supplemented by state-averaged single-point calculations at a higher level. Fig. 5(a) shows CASPT2//CASSCF results based on a large active space, chosen such that a broad spectrum of excited states from NCN_3 to the NCN + N_2 asymptote is adequately described, whereas panel b displays the results of a more accurate MRCI//CASPT2 calculation with a smaller (10e,10o) active space (see section II) and a smaller set of states in the state-averaged CASSCF reference wavefunction.

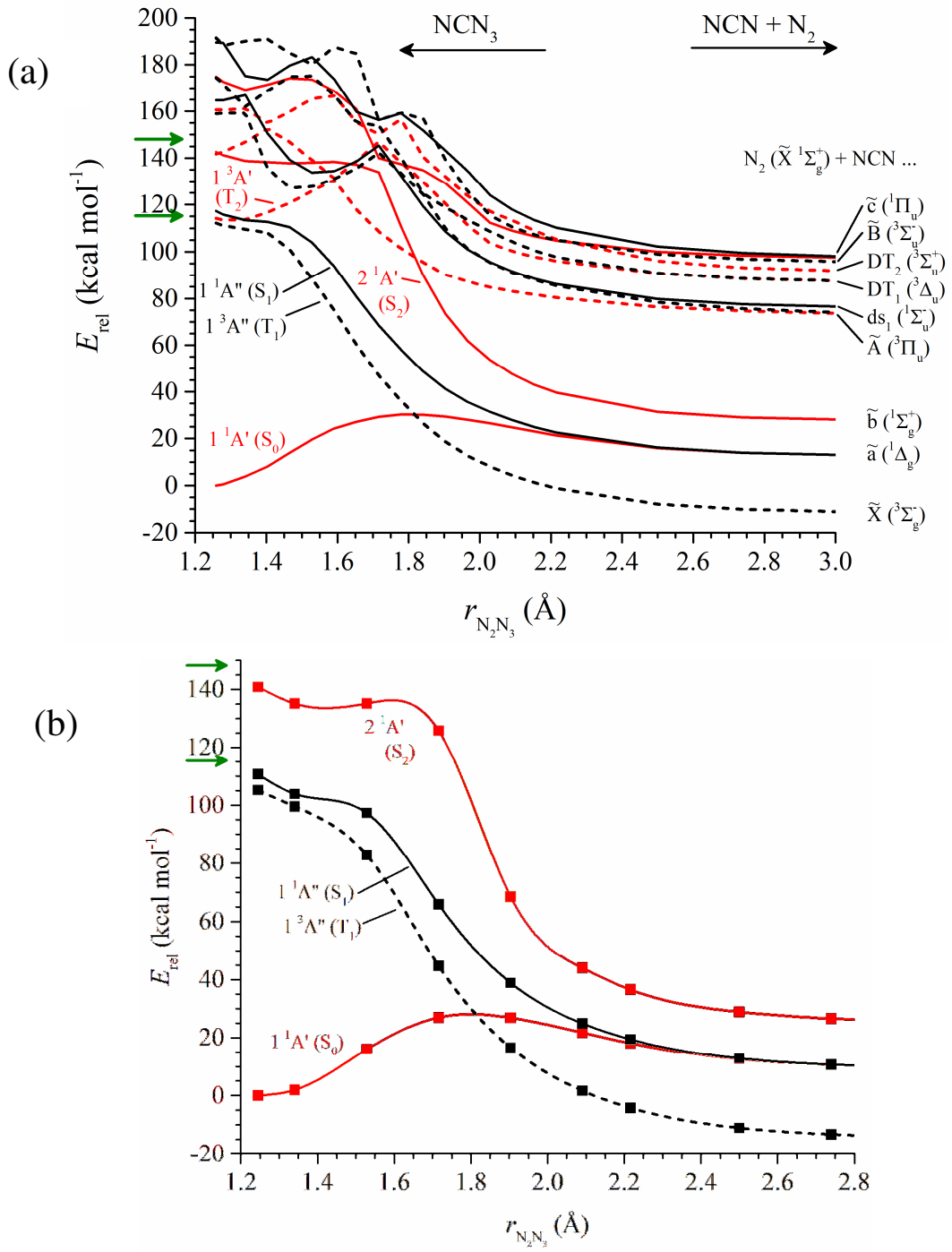

FIG. 5. Correlation of NCN_3 electronic states with those of the dissociation products NCN + N_2, calculated with (a) CASPT2(18e,14o)/def2-TZVP//CASSCF(10e,10o)/def2-TZVP and (b) MRCI(10e,10o)/aug-cc-pVTZ//CASPT2(10e,10o)/aug-cc-pVTZ. Red lines: A′, black lines: A″, solid lines: singlet states, dashed lines: triplet states. Green arrows next to the energy scale: Photon energy of 193 nm (upper) and 248 nm (lower) radiation.

At the NCN_3 geometry ($r_{N_2N_3} = 1.25$ Å), three singlet states (solid lines) below 150 kcal mol^{-1} were found: the $1^1A'$ ground state (S_0) and the first excited $1^1A''$ state (S_1), which both correlate with the degenerate $\tilde{a}\ ^1\Delta_g$ state of NCN in the asymptotic limit, as well as the second excited $2^1A'$ state (S_2) that correlates with $\tilde{b}\ ^1\Sigma_g^+$. All examined states were found to correlate with the ground state of N_2 ($\tilde{X}\ ^1\Sigma_g^+$) for $r \rightarrow \infty$; a channel towards NCN ($\tilde{X}\ ^3\Sigma_g^-$) + N_2 ($\tilde{A}\ ^3\Sigma_u^+$) as proposed by Okabe and Mele[71] could not be confirmed in this study, at least not in the considered energy range. Both S_1 and S_2 are energetically accessible with 193 nm radiation (upper green arrow in Fig. 5 (a)). In addition, four different triplet states, T_1-T_4, are located below this photon energy in the reactant region of the configuration space.

After photo-excitation from S_0 to S_1 or S_2, dissociation can either take place on their repulsive PESs, or radiation-less transitions to T_1-T_4 or S_0 can occur, potentially leading to fragmentation, too. Therefore, direct formation of ^{3}NCN (both as $\tilde{X}\ ^3\Sigma_g^-$ and $\tilde{A}\ ^3\Pi_u$) from NCN_3 photolysis at 193 nm is conceivable. If only spin-allowed pathways are considered, ^{1}NCN can be formed either in the lowest $\tilde{a}\ ^1\Delta_g$ state (via S_0, S_1) or the $\tilde{b}\ ^1\Sigma_g^+$ state (via S_2). Electronic transition dipole moments of 0.24 D for $S_1 \leftarrow S_0$ and 2.44 D for $S_2 \leftarrow S_0$ were calculated at the CASSCF(10e,10o)/aug-cc-pVTZ level, supporting the notion that both channels can be significant. The quantitative prediction of the $\tilde{a}/\tilde{b}$ branching ratio would require not only the determination of relative absorption intensities of S_1 and S_2 at 193 nm including vibrational effects, but also the calculation of quantum yields for both dissociation channels. Such calculations are beyond the scope of the current study.

For λ = 248 nm (lower arrow), the photon energy is clearly below $E(S_2)$ and slightly below $E(S_1)$ at the NCN_3 geometry (Fig. 5, panel a). However, upon increasing the level of theory (Fig. 5, panel b), $E(S_1)$ is decreased beneath the 248 nm threshold (115 kcal mol^{-1}), indicating that the S_1 channel is indeed accessible, in accord with the experimental finding that NCN_3 photo-dissociation takes place at this wavelength.[52] In addition to the initially excited S_1 state, T_1, T_2 and S_0 could be populated after rapid ISC or internal conversion from S_1. T_1 provides a barrier-less pathway towards NCN ($\tilde{X}\ ^3\Sigma_g^-$), whereas a dissociation via T_2 seems unlikely due to the barrier of ca. 15 kcal mol^{-1} in this channel. S_1 and S_0 both lead to N_2 + NCN ($\tilde{a}\ ^1\Delta_g$) so that direct formation of NCN ($\tilde{b}\ ^1\Sigma_g^+$) is not feasible, in contrast to 193 nm photolysis.

From the photon energies and reaction enthalpy, the total initial excess energy of both fragments can be estimated (assuming spin-allowed pathways): 136.4 kcal mol^{-1} (193 nm, N_2 + NCN (ã)), 122.2 kcal mol^{-1} (193 nm, N_2 + NCN ($\tilde{b}$)) and 103.6 kcal mol^{-1} (248 nm, N_2 + NCN (ã)). Regardless of the details of energy partitioning into N_2 and the translational degrees of freedom, nascent ^{1}NCN from photolysis of NCN_3 should be characterized by a significant amount of photochemical activation that may enhance subsequent unimolecular steps such as ISC.

A further interesting feature of the dissociation PESs is the occurrence of a crossing between the S_0 and T_1 surfaces at $r_{N_2N_3} \approx 1.83$ Å, i.e. in the transition state region of the ground state PES. Consequently, a direct thermal ISC route from NCN_3 (S_0) to NCN ($\tilde{X}\ ^3\Sigma_g^-$) + N_2, corresponding to reaction (R2), is conceivable in principle. This could explain *direct* ^{3}NCN formation from thermal NCN_3 dissociation, but not the experimentally observed delayed ^{3}NCN and transient ^{1}NCN signals. The minimum on the seam of crossing (MSX) between S_0 and T_0 was located using the NST code[72] at the CCSD(T)/aug-cc-pVTZ level. In order to compare the energy of this MSX (denoted as MSX1) to the saddle point of the adiabatic reaction on the S_0 surface (denoted as TS), CCF12 calculations were additionally carried out for MSX1. As the exact position of the crossing seam differs in general for different quantum-chemical methods, the optimized MSX structure had to be corrected for the higher-level single-point calculations. Details of this procedure can be found in Appendix A. This yields an MSX1 barrier of 25.2 kcal mol^{-1}, slightly below the adiabatic barrier of 25.7 kcal mol^{-1}.

A non-adiabatic statistical theory (NST) calculation[5,73-76] with "weak-coupling" transition probabilities[77] was carried out for $NCN_3 \rightarrow {}^3NCN + N_2$ (R2) and compared to a conventional RRKM calculation of $NCN_3 \rightarrow {}^1NCN + N_2$ (R4), including Eckart tunneling corrections (see e.g. Ref. 78). In both cases, the rigid-rotor—harmonic oscillator approximation was used. For MSX1, the mass-scaled effective Hessian of both PESs, according to the method of Koga and Morokuma,[79] was diagonalized to obtain the harmonic frequencies. Detailed input parameters for the statistical rate theory calculations can be found in the Supplementary Material.

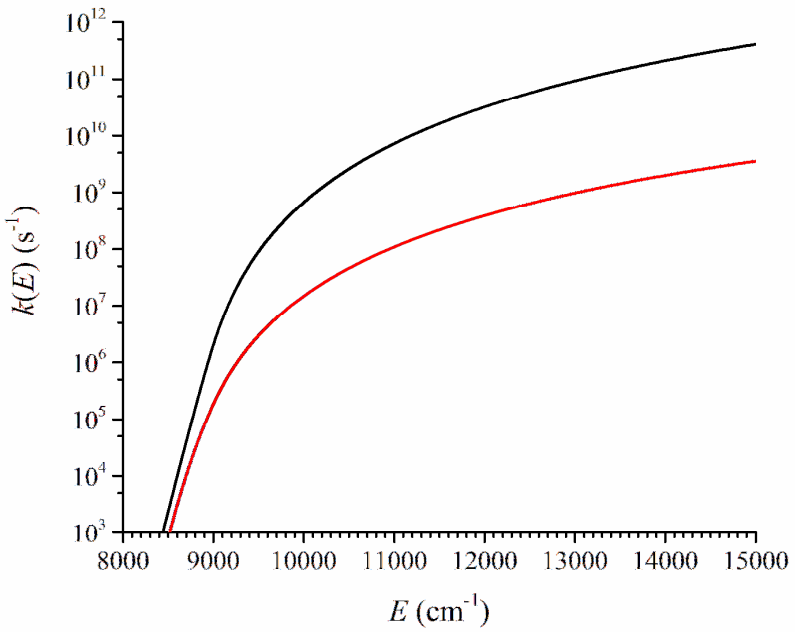

FIG. 6. Microcanonical rate coefficients for NCN_3 dissociation. Black lines: $k_4(E)$, adiabatic pathway $NCN_3 \rightarrow {}^1NCN + N_2$, rate coefficients from RRKM theory with tunneling correction; red lines: $k_2(E)$, spin-forbidden channel $NCN_3 \rightarrow {}^3NCN + N_2$, obtained from NST.

In Fig. 6, the resulting microcanonical rate coefficients $k(E)$ are plotted for the two channels. Note that both rate coefficients are non-zero for energies below the threshold energies of ~9000 cm^{-1} due to the inclusion of tunneling effects in the RRKM and NST calculations. It is evident that the adiabatic reaction dominates over the entire energy range, which is not surprising because of the low transition probability of the spin-forbidden process. Master equation calculations for this two-channel dissociation of NCN_3 confirmed that the spin-forbidden channel contributes only 1-6% to the reaction flux in the temperature range 500-1300 K for pressures between 1 mbar and 10 bar.

For the S_1 PES, it is imaginable that rapid ISC $S_1 \rightarrow T_2$ near the equilibrium geometry takes place after photon absorption, even though this process would compete with the barrier-less adiabatic dissociation on the repulsive S_1 surface. A subsequent internal conversion $T_2 \rightarrow T_1$ could then lead to NCN ($\tilde{X}\ {}^3\Sigma_g^-$). If it is further assumed that $T_2 \rightarrow T_1$ is slow or that vibrational relaxation of ${}^3NCN$ is the rate-determining step, such a mechanism could potentially explain a delayed ${}^3NCN$ signal increase. However, it could not account for the detection of transient ${}^1NCN$ reported in Ref. 51.

B. Surface-Crossing ISC Mechanism for NCN (+M)

One way to rationalize fast ISC processes is the presence of low-lying molecular configurations for which the singlet and triplet states of interest are degenerate. In such a region, transitions between the PESs are typically localized. To identify such surface-crossing regions for NCN, PES scans along the three internal degrees of freedom were performed at the MRCI(14e,12o)/aug-cc-pVTZ level. In Fig. 7, a one-dimensional cut of the surfaces for varying NCN angle θ at constant bond distances r(C-N$_1$) = r(C-N$_2$) = 1.235 Å is depicted. A full-valence (14e,12o) active space was used for these calculations (see also FIG. 1) to encompass a large number of excited states.

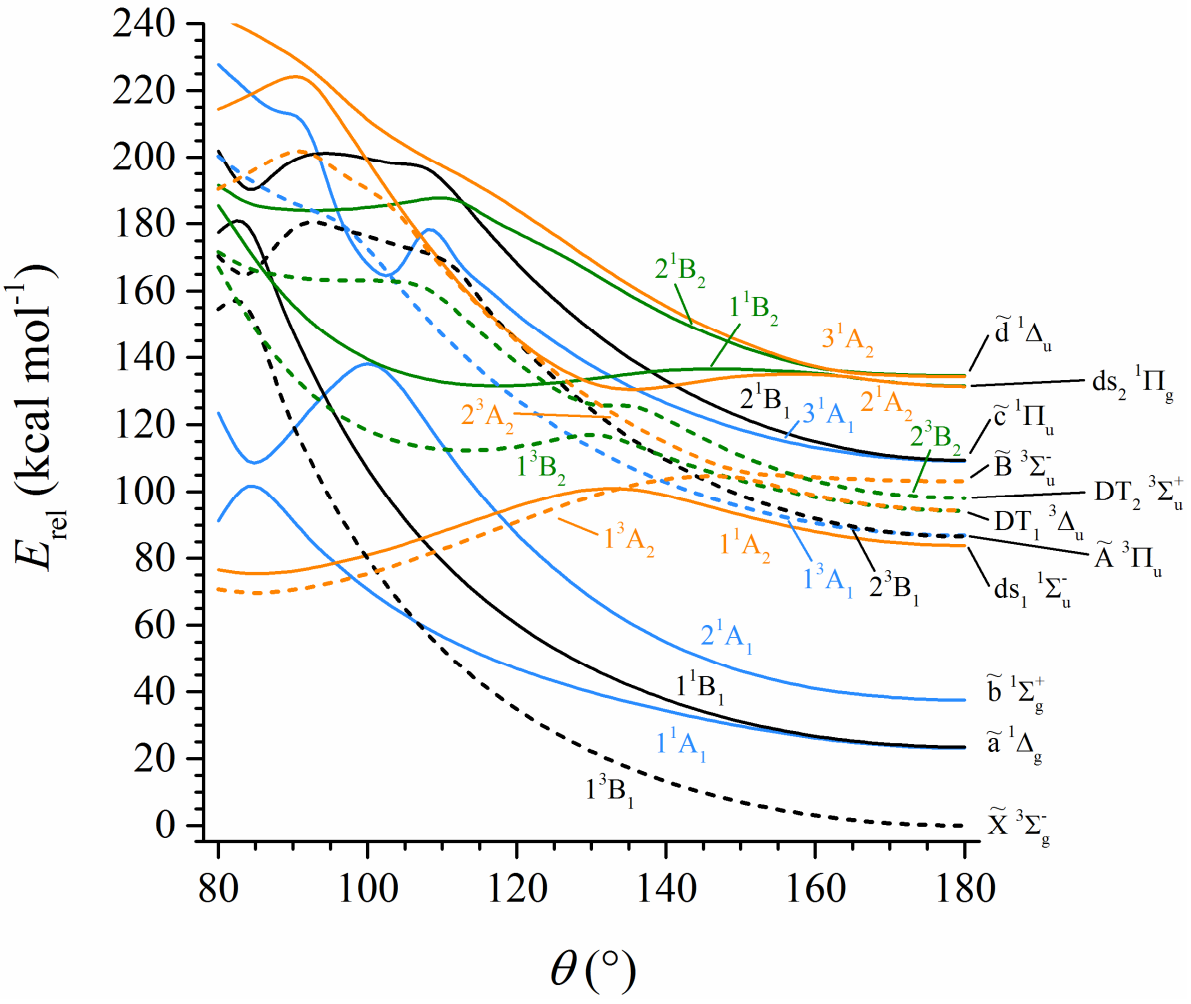

FIG. 7. Angle-dependence of the NCN electronic state energies (C_{2v} symmetry, r_{CN} = 1.235 Å) between 80 and 180° at the MRCI(14e,12o)/aug-cc-pVTZ level. Blue: A_1 symmetry, black: B_1, orange: A_2, green: B_2; solid lines: singlets, dashed lines: triplets.

One salient feature of the curves in Fig. 7 is that they all possess minima at linear geometry, even if some of the higher states (e.g. 1^1A_2, 1^3A_2 and 1^3B_2) have a further minimum at a bent configuration. This impedes the occurrence of low-energy ISCs like for instance in the $^1CH_2/^3CH_2$ system,[80] where the lowest singlet and triplet states possess minima at markedly different H-C-H angles, which facilitates low-energy crossings of the PESs.

As discussed in section III.A, aside from possible direct ^3NCN formation, thermal and photochemical ($\lambda > 203$ nm) dissociation of NCN_3 leads to NCN ($\tilde{a}\ ^1\Delta_g$), where at lower wavelengths NCN ($\tilde{b}\ ^1\Sigma_g^+$) could be an additional or even the dominant product. Therefore, we direct our attention to the $\tilde{X}$, $\tilde{a}$, and $\tilde{b}$ states. Upon bending, the degenerate $\tilde{a}$ singlet state is split into its Renner-Teller (RT) components 1^1A_1 and 1^1B_1 (see also Ref. 41). The lower $^1A_1$ curve intersects with the triplet ground state at an angle of 107° and an energy of 60.7 kcal mol^{-1} relative to the triplet minimum (37.3 kcal mol^{-1} above the singlet minimum). In close vicinity to this crossing, there are two further ISC intersections and two conical intersections, involving the $1\ ^1A_1$, $1\ ^3B_1$, 1^1A_2 and 1^3A_2 states (solid blue, dashed black, solid and dashed orange lines). Depending on the level of theory, the pattern of these nearby crossings can significantly change. For instance, at the CASPT2(10e,10o)/cc-pVDZ level, the crossing between 1^3B_1 and 1^1A_1 (black dashed and blue solid lines in Fig. 7) is found at a *lower* angle than the other four intersections (for a description of the reduced active space, see section II).

The 1^1B_1 component of $\tilde{a}$ and the 2^1A_1 curve (corresponding to $\tilde{b}$) do not intersect with the ground state triplet surface at all (1^1B_1) or only after surmounting a considerable barrier (2^1A_1). There are however intersections with the 1^3A_2 state (dashed orange line) that corresponds to the dark triplet state DT_1 ($^3\Delta_u$) in the linear configuration. These crossings are located at 109° (1^1B_1, 58.4 kcal mol^{-1} above the $\tilde{a}$ minimum) and 119° (2^1A_1, 52.6 kcal mol^{-1} above the $\tilde{b}$ minimum) respectively.

Besides the bending coordinate, the symmetric and antisymmetric stretching coordinates have been considered as well. For these calculations, a reduced (6e,6o) active space containing only the π orbitals has been used. This active space is sufficient to properly describe the lowest set of electronic states. The results of these one-dimensional scans are illustrated in Fig. 8.

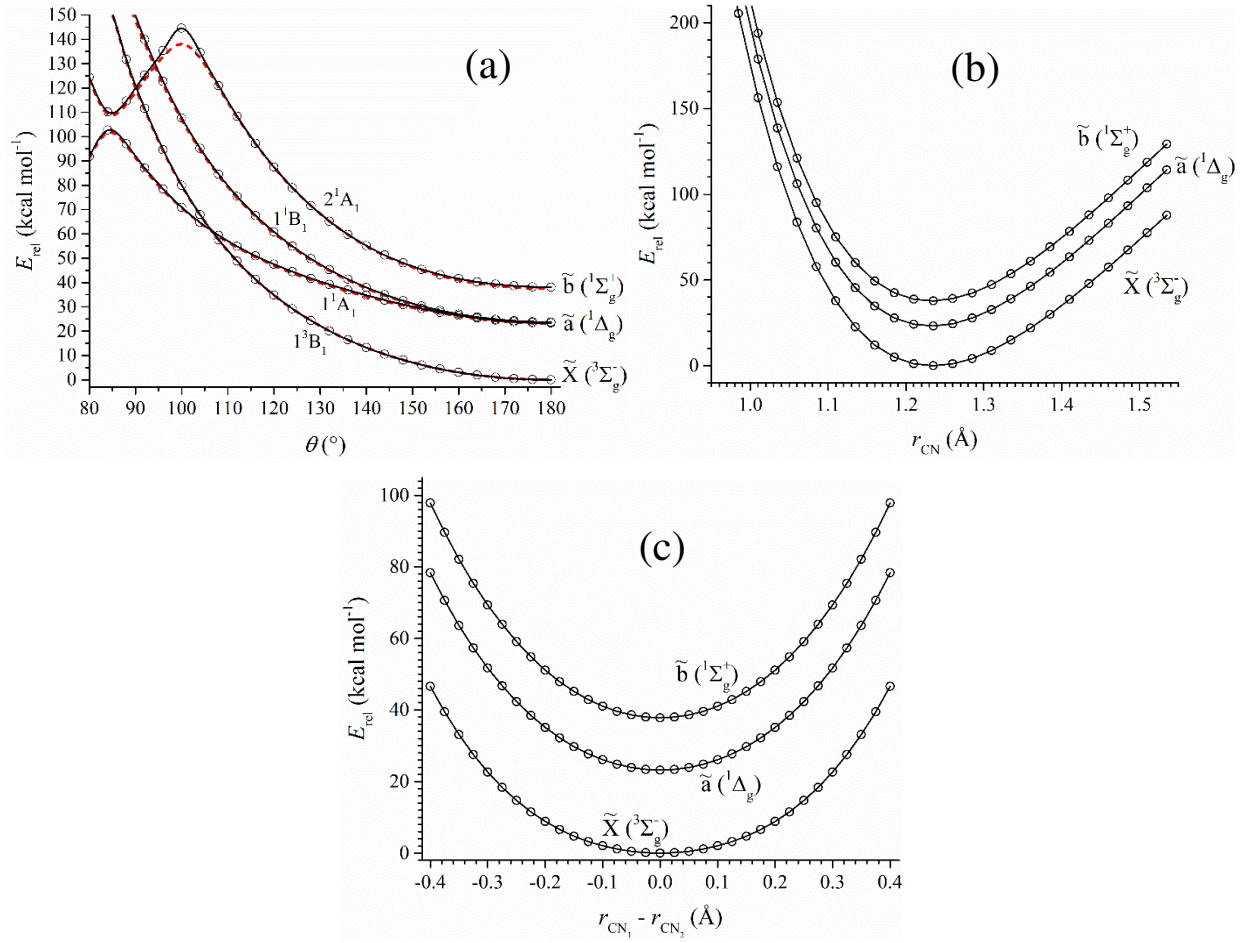

FIG. 8. One-dimensional cross sections of the lowest NCN MRCI(6e,6o)/aug-cc-pVTZ PESs. Panel (a): variation of the bond angle θ, C_{2v} symmetry, r_{CN} = 1.235 Å; panel (b): symmetric variation of the bond distance ($D_{\infty h}$ symmetry, r(C-N$_1$) = r(C-N$_2$)); panel (c): variation of the bond length difference Δr = r(C-N$_1$) - r(C-N$_2$), $C_{\infty v}$ symmetry, $\overline{r_{CN}} = 1/2\left(r_{CN_1} + r_{CN_2}\right) = 1.235$ Å. The red dashed lines in panel (a) illustrate the full-valence MRCI results for comparison.

In panel (a), the full-valence MRCI results (see also Fig. 7) are shown as red dashed lines to demonstrate the very good agreement with the reduced active space result for the bending angle scan. The PES cross sections for the stretching coordinates in panels (b) and (c) feature no intersections between the $\tilde{X}$, $\tilde{a}$ and $\tilde{b}$ states, and the shapes of the curves are very similar to each other. In the Supplementary Material, a correlation diagram for the reaction NCN → CN + N is presented which shows that $\tilde{X}$, $\tilde{a}$ and $\tilde{b}$ correlate with three different asymptotic CN + N sets of states, while their energetic order along the dissociation coordinate is preserved. Thus, the lack of PES crossings for the stretching coordinates is not surprising.

Three-dimensional PES scans on a coarse grid (not shown here) confirmed that the lowest-energy surface crossing occurs between 1^3B_1 and 1^1A_1 at the bent geometry. The corresponding MSX was subsequently located at the MRCI(6e,6o)/aug-cc-pVTZ level. The C_{2v} symmetric structure features bond lengths of 1.227 Å and an angle of 107.0° and is situated 37.8 kcal mol^{-1} above the optimized ã minimum. In the following, it will be denoted as MSX2. A Koga-Morokuma Hessian analysis[79] at MSX2 yielded harmonic frequencies of 1595 (symmetric stretch) and 2605 cm^{-1} (asymmetric stretch) and confirmed that an actual MSX had been found. The asymmetric stretch frequency seems high for a C-N bond, however this anomaly is likely caused by a strongly deformed triplet PES due to the nearby conical intersection of 1^3B_1 and 1^3A_2 (see Fig. 7, black and orange dashed lines).

NST calculations with Landau-Zener transition probabilities were carried out for the thermal unimolecular reaction via MSX2,

$$^1\text{NCN}\ (\tilde{a}\ ^1\Delta_g) + \text{M} \rightarrow {}^3\text{NCN}\ (\tilde{X}\ ^3\Sigma_g^-) + \text{M} \quad \text{(R5)}$$

Detailed input parameters are given in the Supplementary Material. The resulting high-pressure rate coefficients can be described by the following Arrhenius expression in the temperature range between 200 and 1300 K:

$$k_5^\infty(T) = 9.8 \times 10^{11}\text{s}^{-1} \exp\left(-\frac{37.5\ \text{kcal mol}^{-1}}{RT}\right). \quad (1)$$

Exemplary values are $k_5^\infty(240\ \text{K}) = 7 \times 10^{-23}\text{s}^{-1}$, $k_5^\infty(300\ \text{K}) = 5 \times 10^{-16}\text{s}^{-1}$ and $k_5^\infty(600\ \text{K}) = 2 \times 10^{-2}\text{s}^{-1}$. Master equation calculations indicate that the rate coefficients $k(T,P)$ are in the fall-off (low T) or low-pressure (high T) regime and thus significantly lower than the high-pressure limit given in Eq. (1). It is immediately clear from these data that (R5) cannot be responsible for the experimentally observed ISC, which occurs with rates of at least 10^3 s^{-1} even at or below room temperature and exhibits only a weak temperature dependence. The experiments suggest the existence of an ISC pathway with a low barrier, in stark contrast with the 38 kcal mol^{-1} threshold energy of the channel discussed above.

For ^{1}NCN (ã $^1\Delta_g$) produced via photo-dissociation, a chemically activated mechanism could be possible: as mentioned in section III.A, excess energies of greater than 100 kcal mol^{-1} arise from the photo-excitation. It is reasonable to assume that on average at least 50 kcal mol^{-1} remain in the

larger NCN fragment, sufficient to surmount the 38 kcal mol^{-1} barrier of MSX2, provided that collisional stabilization is not dominant. However, this process alone cannot entirely explain the experimental observations for two reasons: (1) fast conversion of ^{1}NCN to ^{3}NCN is also observed for thermal NCN_3 cleavage[17] where chemical activation is not sufficient to overcome the barrier; (2) in the photolysis experiments of Ref. 51, ^{1}NCN ($\tilde{a}\ ^1\Delta_g$) in its vibrational ground state is detected as a transient species that is then further converted to ^{3}NCN. At least in that case, the ISC takes place after the initial activation has already been lost to the environment.

To explore further possible low-energy ISC mechanisms, the interaction of rare gas atoms with NCN has been studied, too. The corresponding van-der-Waals complexes are very weakly bound, with CCF12 well depths (without zero-point corrections) of –0.1, –0.6, –0.7, –0.9 and –0.9 kcal mol^{-1} for He, Ne, Ar, Kr and Xe interacting with ^{3}NCN. The T-shaped equilibrium structures exhibit C-M distances in the range between 3.3 (M = He) and 4.1 Å (M = Xe) and NCN geometries that are virtually identical with the isolated molecule.

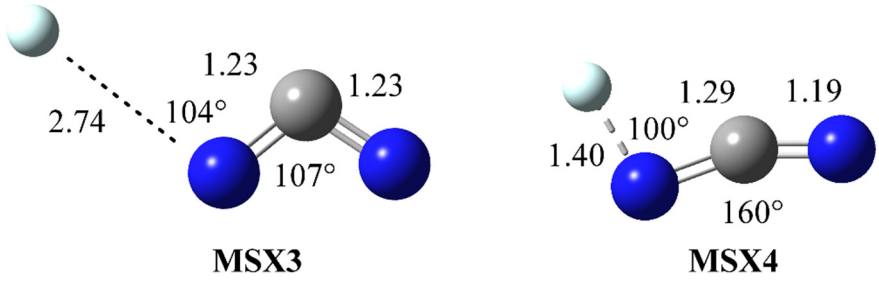

FIG. 9. MSX structures for NCN + He, optimized at the MRCI(6e,6o)/aug-cc-pVTZ level. The interatomic distances are given in units of Å.

For NCN + He, an MSX structure similar to MSX2 was located, with the helium atom coordinating at a distance comparable to the one in the van-der-Waals complex. The geometry of this MSX3 is depicted in Fig. 9. In addition to the long-range MSX3, a further structure with a significantly shorter He-N distance (MSX4, see Fig. 9) was found. The N-C-N bending angle at MSX4 is clearly large than for MSX2 and MSX3, and the C-N bond adjacent to the He atom is significantly elongated compared to the terminal C-N bond. The short N-He distance of 1.40 Å is by far lower than the sum of van-der-Waals radii, 2.95 Å.[81] Thus, MSX4 lies in the repulsive regime of the intermolecular interaction potential, and the surface crossing is presumably a consequence of the triplet state being destabilized more strongly by the interference of the electron clouds.

The barrier for MSX3 relative to the ^{1}NCN + He asymptote amounts to 39.0 kcal mol^{-1}. For MSX4 an even higher barrier of 40.8 kcal mol^{-1} was found. Thus, the presence of He does not lower the barrier to ISC in comparison with an isolated NCN molecule. A simple NST estimate of the rate constant for the He-assisted ISC of ^{1}NCN via MSX3 yields a strong temperature dependence and values well below 10^{-16} cm^3 molecule^{-1} s^{-1} over the entire temperature range of interest. Thus, a helium "catalyzed" surface-crossing mechanism is not suitable for rationalizing the experimental observation of fast ISC, a result that is in line with the weak van-der-Waals interaction between NCN and He.

For the heavier noble gases, similar results as for helium can be expected. In the case of neon, this was confirmed by MSX optimizations with the smaller cc-pVDZ basis set. Furthermore, from the measured rate coefficients it is evident that He is by far the most efficient collider gas for ^{1}NCN quenching in its group.[52] Therefore, no further attempts to locate surface-crossing channels for the higher noble gases were undertaken.

We also considered the possible role of bimolecular reactions of ^{1}NCN with itself or with the precursor NCN_3 for ISC. In all of the published experimental studies on ISC of ^{1}NCN, initial NCN_3 concentrations in the range of 10^{13}-10^{14} molecules cm^{-3} were employed.[17,51,52] This is the upper limit of the sum of NCN_3, ^{1}NCN and ^{3}NCN concentrations at any time during the experiments. In Ref. 52, it is explicitly mentioned that variation of $[NCN_3]_0$ did not influence the observed kinetics, which suggests a negligible contribution of bimolecular chemistry. However, independence of initial concentrations could also be an indicator of a bimolecular process that is so fast that its concentration dependence is not reflected by the measured rate coefficients. If we assume a rapid bimolecular process X + Y with a rate coefficient near the collision limit, k_{coll} = 1.5–3 × 10^{-10} cm^3 molecule^{-1} s^{-1}, the relative consumption rate of species X is $1/[\mathrm{X}] \times \mathrm{d}[\mathrm{X}]/\mathrm{d}t = -k_{\mathrm{coll}}[\mathrm{Y}]$. By assuming $[\mathrm{Y}] \approx [\mathrm{NCN_3}]_0$ at any reaction time, one definitely overestimates the rate of such a bimolecular step. With $[\mathrm{NCN_3}]_0 = 10^{13} - 10^{14}$ cm^{-3}, a relative consumption in the range 1.5 × 10^3 – 3 × 10^4 s^{-1} is obtained from this estimate. For most of the experimental conditions, this estimated rate is *lower* than the observed first-order rate coefficients for ^{1}NCN consumption and ^{3}NCN formation, respectively. Due to the generous nature of the above estimate ($[\mathrm{Y}] \approx [\mathrm{NCN_3}]_0$ and $k \approx k_{coll}$), the actual bimolecular rates will be even lower. Thus, it is very unlikely that NCN self-reactions or NCN + NCN_3 are responsible for rapid ISC under the conditions relevant for the

measurements. For NCN + NCN, a state correlation diagram is presented in the Supplementary Material. It demonstrates that low-energy surface crossings which potentially convert ^{1}NCN to ^{3}NCN do exist for this system. However, these ISC processes are still not barrierless and are therefore unlikely to proceed at collision-controlled rates.

C. Gateway-State ISC Mechanism for NCN (+M)

In the gateway or mixed-state model by Freed and co-workers,[82-84] the problem of describing CIISC is approached from a different direction. The central idea is that rovibrational states of the singlet electronic state can mix with those of the triplet state in the isolated molecule. As a consequence, each singlet rovibrational state possesses a partial triplet character and vice versa. For this mixing to be effective, the pure-spin rovibrational states of different multiplicity have to be close in energy, and they must be strongly coupled by the spin-orbit operator. States with particularly large admixture of a wave function of different multiplicity can serve as so-called gateway states for the CIISC. The collider gas acts as a time-dependent perturbation via its intermolecular force on the molecule of interest. In the absence of mixed states, the intermolecular molecule-collider potential induces vibrational and rotational energy transfer. It can be shown[84] that in the presence of the above-mentioned interelectronic state couplings, a certain fraction of the excited-state rovibrational relaxation rate is "borrowed" to the CIISC process, similar to the concept of intensity borrowing in molecular spectroscopy.[85] The mixed-state model has been successfully applied to CIISC for instance in CH_2 by Temps and co-workers[80,86] and their predictions were later experimentally confirmed by Gannon et al.[87]

For spin-orbit coupling to be symmetry-allowed, the direct product of the irreducible representations of both electronic states must contain one of the rotational operators R_x, R_y or R_z.[88,89] Thus, spin-orbit coupling between $\tilde{X}\ ^3\Sigma_g^-$ and $\tilde{a}\ ^1\Delta_g$ is symmetry-forbidden in the linear NCN configuration. Nevertheless, this restriction is lifted if the symmetry is lowered from $D_{\infty h}$ to C_{2v} by allowing the molecule to bend. Then 1^3B_1 ($\tilde{X}$) can interact with the lower 1^1A_1 RT component of $\tilde{a}$. The resulting angle-dependent spin-orbit matrix element $H_{so}(\theta)$ is plotted in Fig. 10. An increase of H_{so} from 0 at 180° to a maximum of 17.6 cm^{-1} at an angle of 114° is observed.

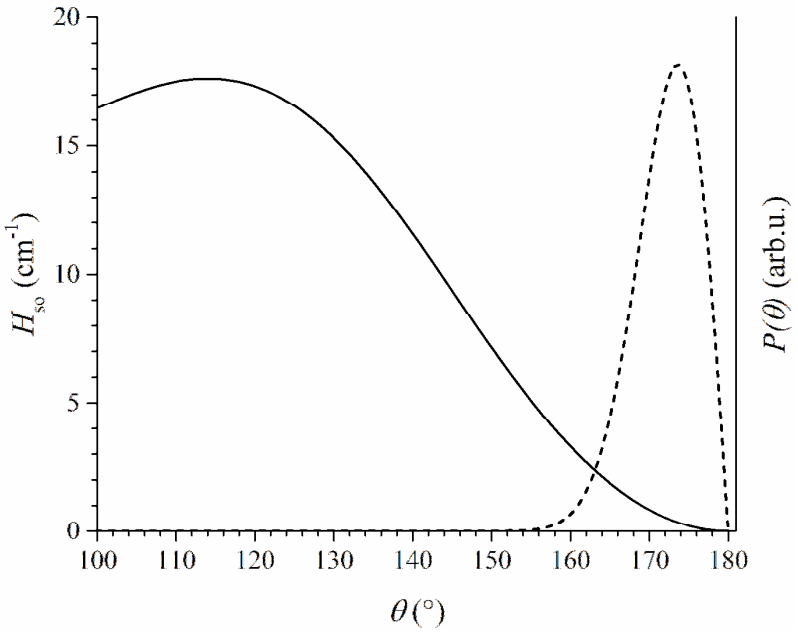

FIG. 10. Angle-dependence of the spin-orbit matrix element $H_{\mathrm{so}} = \langle 1\ ^3\mathrm{B}_1 | \widehat{\mathrm{H}}_{\mathrm{so}} | 1\ ^1\mathrm{A}_1 \rangle$ at constant bond distances 1.235 Å (solid line), obtained at the CASSCF(10e,10o)/aug-cc-pVTZ level with the Breit-Pauli operator (for information on the active space, see section II). Dashed line: Probability density $P(\theta) = \sin\theta \int_0^{2\pi} |\psi_{\mathrm{bend}}(\theta, \varphi)|^2 \, \mathrm{d}\varphi$ of the bending vibrational ground-state wave function of NCN ($\tilde{\mathrm{X}}\ ^3\Sigma_g^-$) (see text for the underlying rigid bender model).

The dashed line in Fig. 10 illustrates the angle-dependent probability density $P(\theta)$ of the vibrational ground-state wave function. It shows that even without any thermal excitation, the bending wave function extends over a range from ca. 155 to 180°. Therefore, regions with non-zero H_{so} are intrinsically accessible to the molecule.

Thus, one then has to consider the matrix elements of the spin-orbit operator over the rovibronic wave functions in order to obtain information about spin-orbit coupling in the rotating and vibrating molecule:[80,90]

$$W_{\mathrm{so}} = \left\langle \psi_{\mathrm{rve}}^{\mathrm{trip}} \middle| \widehat{\mathrm{H}}_{\mathrm{so}} \middle| \psi_{\mathrm{rve}}^{\mathrm{sing}} \right\rangle \approx \left\langle \psi_{\mathrm{str}}^{\mathrm{trip}} \middle| \psi_{\mathrm{str}}^{\mathrm{sing}} \right\rangle \left\langle \psi_{\mathrm{rb}}^{\mathrm{trip}} \middle| H_{\mathrm{so}}(\theta) \middle| \psi_{\mathrm{rb}}^{\mathrm{sing}} \right\rangle, \quad (2)$$

where W_{so} is the effective spin-orbit matrix element, ψ_{rve} are the total rovibronic wave functions, ψ_{str} the stretching vibration wave functions, ψ_{rb} the rotation-bending wave functions and $H_{\mathrm{so}}(\theta)$ is the angle-dependent electronic spin-orbit matrix element (see Fig. 10). Eq. (2) implies the approximation that H_{so} is independent of the bond lengths and that the stretching degrees of freedom can be separated from the bending-rotation motion.

The stretching wave functions can be further separated into a symmetric and antisymmetric part, $\psi_{\mathrm{str}} = \psi_{\mathrm{s}}\psi_{\mathrm{as}}$, so that the stretching overlap integral in Eq. (2) reduces to a product of 1D Franck-Condon integrals $\left\langle \psi_{\mathrm{str}}^{\mathrm{trip}} \middle| \psi_{\mathrm{str}}^{\mathrm{sing}} \right\rangle = \left\langle \psi_{\mathrm{s}}^{\mathrm{trip}} \middle| \psi_{\mathrm{s}}^{\mathrm{sing}} \right\rangle \left\langle \psi_{\mathrm{as}}^{\mathrm{trip}} \middle| \psi_{\mathrm{as}}^{\mathrm{sing}} \right\rangle$. The (anti-)symmetric stretching wave functions were expressed in a basis of harmonic oscillator (HO) functions:

$$\psi_{\mathrm{s/as},i} = \sum\nolimits_j \nu_{\mathrm{s/as},ij} \psi_{\mathrm{s/as},j}^{(\mathrm{HO})}. \quad (3)$$

The coefficients ν were obtained by solving the corresponding one-dimensional variational problem with an anharmonic potential of the form $V(q) = 1/2\, kq^2 + a_3 q^3 + a_4 q^4 + a_5 q^5 + a_6 q^6$, where q denotes the (anti-)symmetric stretching normal coordinate. The coefficients k and a_i were determined by polynomial fits of the 1D PES scans (see panels b, c of Fig. 8). Due to Eq. (3), the Franck-Condon integrals $\left\langle \psi_{\mathrm{s/as}}^{\mathrm{trip}} \middle| \psi_{\mathrm{s/as}}^{\mathrm{sing}} \right\rangle$ of the anharmonic stretching wave functions are reduced to a linear combination of HO overlap integrals. While it is possible to calculate these analytically,[91] a simple trapezoidal integration with sufficient grid points proved to be more stable over a large range of vibrational quantum numbers. For the symmetric stretching vibration, the slight shift of equilibrium C-N bond lengths $\Delta r < 0.002$ Å between ^{3}NCN and ^{1}NCN was neglected.

The rotation-bending wave functions ψ_{rb} were treated in the rigid-bender approximation,[92] with details of the calculation described in Appendix B. It must be emphasized that this rather crude model is not expected to achieve spectroscopic accuracy in this case but instead to give a reasonable qualitative picture of the large-amplitude bending vibration that strongly influences the spin-orbit coupling. All input data for the rigid-bender and stretching anharmonic oscillator models are compiled in the Supplementary Material.

Within the rigid-bender model, the rotation-bending functions are expressed in a basis $|J\ K\ l\ n\rangle$ (see Appendix B). The spin-orbit matrix elements over the rotation-bending functions then read as (see Ref. 90):

$$\left\langle \psi_{\mathrm{rb}}^{\mathrm{trip}} \middle| H_{\mathrm{so}}(\theta) \middle| \psi_{\mathrm{rb}}^{\mathrm{sing}} \right\rangle = \sum\nolimits_{n,l,n',l'} d_{\mathrm{trip}}^{NK'l'n'} d_{\mathrm{sing}}^{JKln} \langle NK'|JK\rangle \langle l'n'|H_{\mathrm{so}}(\theta)|l\ n\rangle. \quad (4)$$

Here, J is the total angular momentum of the singlet, N is the spin-free rotational quantum number of the triplet, and $K^{(\prime)}$ is the projection of these quantum numbers on the principal axis of the molecule. The quantum number l corresponds to the vibrational angular momentum, and the degree of the Legendre polynomials in the basis functions is defined by n. The evaluation of spin-orbit matrix elements over the bending basis functions $|l\, n\rangle$ is straightforward if $H_{\mathrm{so}}(\theta)$ is expressed as a linear combination of Legendre polynomials in $\cos\theta$, in analogy with the bending potential for the solution of the rigid-bender problem (see Eq. (20) in Appendix B). One then has to solve integrals of products of three associated Legendre polynomials, a problem for which analytical solutions exist.[93,94] The rotational factors $\langle NK'|JK\rangle$ were evaluated according to the expressions derived by Stevens and Brand.[95] The corresponding selection rules are $\Delta N = 0, \pm 1$ and $\Delta K = 0, \pm 1$ for the interacting states. Furthermore, $\Delta K = 0$ interactions can only occur when the direct product of the vibronic symmetry of the participating states corresponds to the rotational operator R_z, while $\Delta K = \pm 1$ interactions are only possible if this product contains R_x or R_y.[95]

A further complication arises due to the fact that NCN exists in ortho and para configurations according to the nuclear spin $I = 1$ of ^{14}N. The relative abundance of the ortho state (total nuclear spin $T = 0, 2$) is twice as large as that of the para state ($T = 1$). As a consequence of the Pauli principle, ortho NCN can only exist in states with a symmetric rotational function while for para NCN, only antisymmetric functions are possible.[89] In principle, ortho and para NCN have to be treated as separate chemical species, with distinct symmetry restrictions for both. As a simplification, in this work no explicit distinction between ortho and para NCN was made. However, an additional symmetry restriction on the state interactions was imposed, such that only nuclear spin-allowed pairs of states were considered.

To search for gateway state candidates, for each quantum number J of the singlet state, a complete set of rotation-bending-stretching states with energies

$$E_i^{\mathrm{sing}} = \Delta E_{\mathrm{T\rightarrow S}} + \epsilon_{\mathrm{rb},i}^{\mathrm{sing}} + \epsilon_{\mathrm{str},i}^{\mathrm{sing}}, \quad (5)$$

up to a maximum energy of 11,000 cm^{-1} was considered. Here, $\Delta E_{\mathrm{T\rightarrow S}}$ is the experimentally determined triplet-singlet splitting of 8150 cm^{-1},[33] and $\epsilon_{\mathrm{rb},i}$ and $\epsilon_{\mathrm{str},i}$ are the rotation-bending and stretching eigenvalues. Corresponding sets of states with $E_i^{\mathrm{trip}} = \epsilon_{\mathrm{rb},i}^{\mathrm{trip}} + \epsilon_{\mathrm{str},i}^{\mathrm{trip}}$ were then calculated for the triplet ground state. Due to the spin-orbit coupling selection rules, this has to be

only done for $N_{\mathrm{trip}} = J_{\mathrm{sing}} - 1, J_{\mathrm{sing}}, J_{\mathrm{sing}} + 1$. Then all singlet-triplet pairs with an energy difference less than 500 cm^{-1} and a coupling element W_{so} greater than 10^{-5} cm^{-1} were automatically selected and output. The energy criterion was deliberately chosen very loosely to account for possibly large errors in the internal energy eigenvalues due to the crude model employed. This procedure was repeated for $J_{\mathrm{sing}} = 0 \ldots 70$ to cover a broad range of thermally accessible states.

TABLE I. Exemplary results of the gateway-state screening for $J_{\mathrm{sing}} = 3$, $N_{\mathrm{trip}} = 2$ up to $E_{\mathrm{trip}} = 9400\ \mathrm{cm}^{-1}$. v_1 and v_3 are the symmetric and antisymmetric stretching quantum numbers, i_{rb} denotes the index of the energy-ordered rigid-bender states. $E_{\mathrm{sing/trip}}$ are the singlet/triplet energies relative to the triplet vibrational ground state. W_{so} is the spin-orbit coupling calculated with Eq. (2).

v_1^{sing}	v_1^{trip}	v_3^{sing}	v_3^{trip}	$i_{\mathrm{rb}}^{\mathrm{sing}}$	$i_{\mathrm{rb}}^{\mathrm{trip}}$	$E_{\mathrm{sing}}/\mathrm{cm}^{-1}$	$E_{\mathrm{trip}}/\mathrm{cm}^{-1}$	$W_{\mathrm{so}}/\mathrm{cm}^{-1}$
0	0	0	4	1	7	8153	7851	-0.00008
0	0	0	0	1	44	8153	8054	0.00032
0	0	0	0	1	46	8153	8059	0.00007
0	0	0	4	1	9	8153	8283	0.00002
0	0	0	4	1	11	8153	8285	0.00003
0	0	0	2	1	29	8153	8451	0.00003
0	0	0	4	2	8	8153	7851	-0.00009
0	0	0	0	2	45	8153	8054	0.00032
0	0	0	4	2	10	8153	8283	0.00002
0	0	0	2	2	30	8153	8451	0.00003
0	0	0	4	3	9	8578	8283	-0.00004
0	0	0	4	3	11	8578	8285	-0.00023
0	0	0	4	3	12	8578	8720	-0.00009
0	0	0	4	4	10	8578	8283	0.00005
0	0	0	4	5	9	8593	8283	-0.00020
0	0	0	4	5	11	8593	8285	-0.00002
0	0	0	4	6	10	8593	8283	-0.00020
0	0	0	4	7	12	8993	8720	0.00060
0	0	0	4	7	14	8993	9157	0.00006
0	0	0	4	7	16	8993	9159	-0.00015
0	0	0	4	8	13	9015	8720	0.00004
0	0	0	0	8	50	9015	9001	-0.00004
0	0	0	4	9	12	9017	8720	-0.00016
0	0	0	0	9	49	9017	9001	0.00028
0	0	0	0	9	51	9017	9006	0.00006
0	0	0	4	9	14	9017	9157	-0.00003
0	0	0	4	9	16	9017	9159	0.00007
0	0	0	2	9	34	9017	9367	0.00002
0	0	0	4	10	13	9017	8720	0.00023
0	0	0	0	10	50	9017	9001	-0.00029
0	0	0	4	10	15	9017	9157	0.00002
0	0	0	2	10	35	9017	9367	-0.00002

An example of the results of this selection routine is shown in Table I (for $J_{\mathrm{sing}} = 3$ and $N_{\mathrm{trip}} = 2$). The outcome can be regarded as typical for the complete range of rotational quantum numbers, although the number of states naturally increases strongly with J. There are no low-energy state pairs with both an appreciable coupling element W_{so} (on the order of 1 cm^{-1} or greater, see e.g. Ref. 90) and a near degeneracy. The largest W_{so} found in this study was 0.12 cm^{-1}, with singlet and triplet energies of 11440 and 10950 cm^{-1} respectively, corresponding to an energy gap of 490 cm^{-1} and an internal energy of 3290 cm^{-1} (9.4 kcal mol^{-1}) for the singlet state.

The weak interaction can be readily understood qualitatively in terms of the large energy gap between the singlet and triplet ground states and the individual contributions in Eq. (2): The stretching overlap integrals will be large only for vibrational levels with close-by vibrational quantum numbers. This is due to the similar shape of the stretching potentials in both states (see Fig. 8) that causes the vibrational wave functions in one electronic state to be approximately orthogonal to the wave functions in the other state. On the other hand, to bridge the large triplet-singlet splitting $\Delta E_{\mathrm{T}\rightarrow\mathrm{S}}$, there must be a significant difference in internal energy for a near degeneracy to occur. There cannot be a large difference in the rotational excitation because of the selection rules $|\Delta N| = 0, 1$ and $|\Delta K| = 0, 1$. So the only remaining degree of freedom is the bending vibration, which affects the factor $\left\langle \psi_{\mathrm{rb}}^{\mathrm{trip}} \middle| H_{\mathrm{so}}(\theta) \middle| \psi_{\mathrm{rb}}^{\mathrm{sing}} \right\rangle$ in Eq. (2). Similarly to the stretching vibrations, however, a large difference in the bending vibration quantum numbers will cause a small overlap between the vibrational wave functions and thus small values of W_{so}. This situation is significantly different from the prototypical gateway-mechanism system $^1CH_2 \rightarrow {}^3CH_2$, where $\Delta E_{T\rightarrow S}$ is around 2.5 times smaller than for NCN, $H_{\mathrm{so}}(\theta)$ is consistently large in the relevant range of bending angles, and the equilibrium structures of both states are so different ($\theta = 133°$ and $102°$) that a large overlap between bending functions with very different quantum numbers is observed.[80,90] While a gateway-type mechanism cannot be completely excluded for NCN, the computational results of this study indicate that it is very unlikely that strongly mixed states for X̃/ã exist. Laser magnetic resonance spectroscopy, which was also applied in the case of $^1CH_2/^3CH_2$,[90] might be able to resolve this question by directly probing mixed states within the singlet manifold.

IV. CONCLUSION

The first part of the present study focused on the dissociation mechanism of NCN_3 upon thermal and photo activation. For the thermal process, adiabatic fragmentation forming NCN ($\tilde{a}\ ^1\Delta_g$) competes with spin-forbidden dissociation to NCN ($\tilde{X}\ ^3\Sigma_g^-$) via a surface crossing of the lowest singlet and triplet states. The calculated rate coefficients of these channels indicate that direct ^{3}NCN formation from NCN_3 pyrolysis is a minor process and NCN ($\tilde{a}\ ^1\Delta_g$) is the main first-generation product. For NCN_3 photolysis on the other hand, direct ^{3}NCN formation is conceivable via ISC to one of the triplet states that are energetically close to the initially populated NCN_3 singlet state(s). Within the spin-allowed photolysis channels, NCN ($\tilde{a}\ ^1\Delta_g$), the lowest singlet state, is the only product for $\lambda > 203$ nm, while additional formation of NCN ($\tilde{b}\ ^1\Sigma_g^+$) is likely to play a role at lower wavelengths.

The investigation of PES crossings between $\tilde{a}$, $\tilde{b}$ and the triplet ground state ($\tilde{X}$) of NCN revealed a potential ISC pathway ^{1}NCN ($\tilde{a}$) → ^{3}NCN ($\tilde{X}$) via a strongly bent configuration (107°). However, the barrier of 37.8 kcal mol^{-1} relative to the linear ^{1}NCN minimum turned out to be far too high to explain the experimentally observed fast ISC rates. For the $\tilde{b}$ state, no analogous channel exists. The interaction of helium with NCN gives rise to an ISC channel similar to the one in the isolated NCN molecule, as well as a short-range surface crossing in the repulsive region of the potential. The barriers for both crossings are at least as high as in the case of isolated NCN, thus they can be excluded as candidates for fast ISC pathways, too. The exploration of rovibrational states of mixed-multiplicity character—so-called gateway states—yielded no pairs of states that are nearly degenerate and strongly coupled by spin-orbit interaction at the same time ($\tilde{a} \leftrightarrow \tilde{X}$). This can be explained by the large energy gap, nearly identical equilibrium geometries and similar vibrational potentials, as well as the electronic spin-orbit matrix element that is small near the minimum geometry due to symmetry restrictions. Thus, neither the surface-crossing nor the gateway mechanism seem to be appropriate to explain the experimental observation of a fast, nearly temperature-independent ISC pathway.

So far, the reason for the apparent discrepancy between theory and experiment remains unclear. The experimental data suggest that a low-barrier ISC pathway exists. It is possible that the theoretical picture that we tried to obtain in this study is far from complete, or that an ISC mechanism involving neither surface crossings nor gateway states is operative in this case. On the

other hand, it cannot be completely ruled out that the measurements involve some undesired secondary chemistry, e.g. wall reactions or reactions induced by the radiation of the detection lasers. It would certainly be interesting to see if the same relaxation dynamics would be observed for alternative methods of NCN generation. Further, a more detailed spectroscopic investigation of the transient ^{1}NCN species could help to estimate its initial activation in order to prove or exclude a chemically activated ISC mechanism.

SUPPLEMENTARY MATERIAL

See supplementary material for coordinates, vibrational frequencies, rotational constants, active space information and visualization, correlation diagrams for NCN + NCN and CN + N, NST input parameters and model parameters for the rigid-bender/stretching anharmonic oscillator calculations.

ACKNOWLEDGEMENTS

Mark Pfeifle would like to thank the German Academic Exchange Service (Deutscher Akademischer Austauschdienst, DAAD) for a postdoctoral grant. This material is based upon work supported by the U.S. Department of Energy, Office of Science, Office of Basic Energy Sciences, Division of Chemical Sciences, Geosciences, and Biosciences under Contract No. DE-AC02-06CH11357DOE-BES through the GPCP program. Further development of our NST codes was supported by the AITSTME project as part of the Predictive Theory and Modeling component of the Materials Genome Initiative (now under the CTC program of DOE-BES).

APPENDIX A: CORRECTION OF MSX STRUCTURE FOR A HIGHER-LEVEL SINGLE-POINT CALCULATION BASED ON A LOWER-LEVEL OPTIMIZED GEOMETRY

When single-point energy calculations are carried out with a higher-level electronic structure method at an MSX geometry that was optimized with a lower-level method, the energies of the triplet and singlet states will in general not coincide at the higher level because the location of the crossing seam will slightly differ for the different methods. One way to overcome this problem is to use a hybrid MSX optimization scheme as proposed by Harvey et al.[96] In short, the problem of finding an MSX is equivalent to finding a stationary point of the Lagrangian $L(\mathbf{x}, \lambda) = V_1(\mathbf{x}) +$

$\lambda[V_2(\mathbf{x}) - V_1(\mathbf{x})]$, where $V_i(\mathbf{x})$ are the electronic energies of the two states as a function of nuclear configuration **x**. This gives rise to the following conditions for the MSX:

$$\mathbf{g}_1(\mathbf{x}) + \lambda[\mathbf{g}_2(\mathbf{x}) - \mathbf{g}_1(\mathbf{x})] = 0, \tag{6}$$

$$V_1(\mathbf{x}) = V_2(\mathbf{x}). \tag{7}$$

Here, $\mathbf{g}_i = \nabla V_i$ is the gradient of the *i*-th state. In Harvey's hybrid approach, the condition in Eq. (6) is fulfilled for the lower level and the degeneracy condition in Eq. (7) for the higher level of theory. It relies on the assumption that the shapes of the PESs are similar for both methods, whereas the absolute singlet-triplet splitting might differ considerably. The disadvantage of this method is the computational cost because during the MSX optimization, expensive single-point calculations have to be performed in each iteration in addition to the gradient calculations at the lower level.

In this work, a simplified version of this hybrid model was applied to MSX1, the MSX for NCN_3 dissociation. First, the MSX was optimized at the lower level in the usual way and the Hessians of both states, $\mathbf{H}_1$ and $\mathbf{H}_2$, were calculated for the harmonic frequency analysis. An additive one-step correction **y** was then applied to the initial structure **x*** by invoking the following approximations for the gradients and energies in Eqs. (6) and (7):

$$\mathbf{g}_i(\mathbf{x}^* + \boldsymbol{y}) \approx \mathbf{g}_i^{\mathrm{lo}}(\mathbf{x}^*) + \mathbf{H}_i^{\mathrm{lo}}\mathbf{y} \text{ and} \tag{8}$$

$$V_i(\mathbf{x}^* + \boldsymbol{y}) \approx V_i^{\mathrm{hi}}(\mathbf{x}^*) + \mathbf{y}^{\mathrm{T}}\mathbf{g}_i^{\mathrm{lo}}(\mathbf{x}^*) + \frac{1}{2}\mathbf{y}^{\mathrm{T}}\mathbf{H}_i^{\mathrm{lo}}(\mathbf{x}^*)\mathbf{y}. \tag{9}$$

Here, 'lo' and 'hi' denote the lower and higher levels of theory. This leads to the following expression for the correction **y** as a function of λ (Eq. (6) combined with Eq. (8)):

$$\mathbf{y}(\lambda) = -\left[\mathbf{H}_1^{\mathrm{lo}}(1-\lambda) + \mathbf{H}_2^{\mathrm{lo}}\lambda\right]^{-1}\left[\mathbf{g}_1^{\mathrm{lo}}(1-\lambda) + \mathbf{g}_2^{\mathrm{lo}}\lambda\right]. \tag{10}$$

The estimated higher-level energies at **x*** + **y** are obtained by substituting **y** of Eq. (10) into Eq. (9). Using an arbitrary λ will violate the degeneracy condition in general. The actual corrector step can then be found by varying λ until $V_1(\mathbf{x}^* + \boldsymbol{y}) = V_2(\mathbf{x}^* + \boldsymbol{y})$ is fulfilled within the quadratic approximation, Eq. (9). More than one solution for λ may exist. In this case, it is probably most reasonable to choose the one that results in the smallest step size $|\mathbf{y}|$.

The procedure described above corresponds to a Newton-Raphson version of Harvey's hybrid optimization method that is initialized at the lower-level optimized structure and terminated after

exactly one cycle. Therefore, in total only four single-point energy evaluations at the high level are necessary with this simplified method.

In the case of MSX1, the CCF12 energies (higher-level method) relative to NCN_3 were 25.25 kcal mol^{-1} (singlet) and 26.44 kcal mol^{-1} (triplet) at the original CCSD(T)/aug-cc-pVTZ (lower-level) structure **x***. After the correction step, the CCF12 energies were 25.15 kcal mol^{-1} (singlet) and 25.18 kcal mol^{-1} (triplet) respectively. The remaining difference of 0.03 kcal mol^{-1} between the PESs was neglected, and the average of the two values was used in the subsequent rate calculations.

APPENDIX B: SETUP OF THE RIGID-BENDER MODEL AND CALCULATION OF MATRIX ELEMENTS

Similar to the study of Stoecklin et al. on HCN,[97] the rovibrational Hamiltonian by Carter and Handy[98] (quoted from Sutcliffe[99,100]) with fixed C-N distances was used as a basis for describing the rigid-bender problem:

$$\widehat{\mathrm{H}} = \widehat{\mathrm{K}}_{\mathrm{v}} + \widehat{\mathrm{K}}_{\mathrm{vr}} + \widehat{\mathrm{V}}, \quad (11)$$

where $\widehat{\mathrm{K}}_{\mathrm{v}}$ represents the kinetic energy of the bending vibration, $\widehat{\mathrm{K}}_{\mathrm{vr}}$ the vibration-rotation interaction and $\widehat{\mathrm{V}}$ the bending potential. The kinetic energy contributions read as:

$$\begin{aligned}\widehat{\mathrm{K}}_{\mathrm{v}} = &-\frac{\hbar^2}{2}\left[\left(\frac{1}{\mu_1 R_1^2}+\frac{1}{\mu_2 R_2^2}\right)\frac{1}{\sin\theta}\frac{\partial}{\partial\theta}\sin\theta\frac{\partial}{\partial\theta}\right] \\ &+\frac{\hbar^2}{\mu_{12}R_1R_2}\left[\frac{\cos\theta}{\sin\theta}\frac{\partial}{\partial\theta}\sin\theta\frac{\partial}{\partial\theta}+\sin\theta\frac{\partial}{\partial\theta}\right],\end{aligned} \quad (12)$$

$$\begin{aligned}\widehat{\mathrm{K}}_{\mathrm{vr}} = &\frac{1}{2}\left[\left(\frac{1}{\mu_1 R_1^2}\right)\left(\frac{\cos\theta}{\sin\theta}\right)^2+\left(\frac{1}{\mu_2 R_2^2}\right)\frac{1}{\sin^2\theta}-\frac{2\cos\theta}{\sin^2\theta}\left(\frac{1}{\mu_{12}R_1R_2}\right)\right]\widehat{\Pi}^2{}_z \\ &+\left(\frac{1}{2\mu_1 R_1^2}\right)\left(\widehat{\Pi}^2{}_x+\widehat{\Pi}^2{}_y\right) \\ &+\left[\left(\frac{1}{2\mu_1 R_1^2}\right)\frac{\cos\theta}{\sin\theta}-\left(\frac{1}{2\mu_{12}R_1R_2}\right)\frac{1}{\sin\theta}\right]\left(\widehat{\Pi}_x\widehat{\Pi}_z+\widehat{\Pi}_z\widehat{\Pi}_x\right) \\ &+\frac{\hbar}{i}\left\{\left(\frac{1}{\mu_1 R_1^2}\right)\left[\frac{\partial}{\partial\theta}+\frac{\cos\theta}{2\sin\theta}\right]-\left(\frac{1}{2\mu_{12}R_1R_2}\right)\left[\frac{1}{\sin\theta}+2\cos\theta\frac{\partial}{\partial\theta}\right]\right\}\widehat{\Pi}_y,\end{aligned} \quad (13)$$

with the equilibrium C-N bond distances R_1 and R_2 (identical in this case), the NCN bending angle θ and the reduced masses $\mu_1 = \mu_2 = (1/m_\mathrm{C} + 1/m_\mathrm{N})^{-1}$ and $\mu_{12} = m_\mathrm{C}$. The operators $\widehat{\Pi}_i$ are the projections of the total angular momentum operator onto the molecule-fixed axes.

The following basis functions were used to solve the variational problem, in analogy with the work of Sutcliffe and Tennyson[99] and Carter and Handy:[101]

$$|J\ l\ n\rangle = \sqrt{\frac{2J+1}{8\pi^2}} D^J_{0l}(0,\beta,\gamma) \sqrt{\frac{(2n+1)(n-l)!}{2(n+l)!}}\ P^l_n(\cos\theta)\exp(il\phi), \quad (14)$$

where the angle ϕ corresponds to the rotation of the vibrational angular momentum, and β and γ are Euler angles describing the orientation of the body-fixed frame with respect to the space-fixed coordinate system. $P^l_n(\cos\theta)$ are the associated Legendre polynomials and D^J_{0l} the standard angular momentum eigen-functions (Wigner D-functions[102]) with $M = 0$. J is the total rotational quantum number, l the quantum number of the bending rotation and n the order of the associated Legendre polynomials. The quantum number M describing the spatial orientation of J was arbitrarily set to 0 for simplicity as the energy levels do not depend on it. The matrix elements of $\widehat{\mathrm{H}}$ in the basis of Eq. (14) were obtained from the work of Stoecklin et al.,[97] including corrections[103] of misprints in Eqs. (8), (9) and (10) of Ref. 97. For this reason, the corresponding relations will be reproduced again at this point. The vibrational part of the kinetic energy can be split into two terms, $\widehat{\mathrm{K}}_\mathrm{v} = \widehat{\mathrm{K}}^{(1)}_\mathrm{v} + \widehat{\mathrm{K}}^{(2)}_\mathrm{v}$:

$$\left\langle J\ l'\ n'\middle|\widehat{\mathrm{K}}^{(1)}_\mathrm{v}\middle|J\ l\ n\right\rangle = \frac{\hbar^2}{2}\delta_{l,l'}\delta_{n,n'} n(n+1)\left(\frac{1}{\mu_1 R_1^2} + \frac{1}{\mu_2 R_2^2}\right), \quad (15)$$

$$\left\langle J\ l'\ n'\middle|\widehat{\mathrm{K}}^{(2)}_\mathrm{v}\middle|J\ l\ n\right\rangle = -\frac{\hbar^2}{\mu_{12} R_1 R_2}\delta_{l,l'}\delta_{n,n'\pm1}\sqrt{\frac{(n_> + l)(n_> - l)}{(2n_> + 1)(2n_> - 1)}}\, n_>^2, \quad (16)$$

with $n_> = \max(n, n')$. The following matrix elements are obtained for $\widehat{\mathrm{K}}_\mathrm{vr} = \widehat{\mathrm{K}}^{(1)}_\mathrm{vr} + \widehat{\mathrm{K}}^{(2)}_\mathrm{vr}$:

$$\begin{aligned}\left\langle J\ l'\ n'\middle|\widehat{\mathrm{K}}^{(1)}_\mathrm{vr}\middle|J\ l\ n\right\rangle &\\ = \frac{\hbar^2}{2\mu_1 R_1^2}\delta_{n',n}\{&\delta_{l',l}[J(J+1) - 2l^2] - \delta_{l',l+1} C^+_{Jl} C^+_{nl} \\ &- \delta_{l',l-1} C^-_{Jl} C^-_{nl}\},\end{aligned} \quad (17)$$

with $C_{Jl}^{\pm} = \sqrt{J(J+1) - l(l \pm 1)}$ and

$$\begin{aligned}
&\left\langle J\ l'\ n' \middle| \widehat{\mathrm{K}}_{\mathrm{vr}}^{(2)} \middle| J\ l\ n \right\rangle \\
&= \frac{\hbar^2}{2\mu_{12} R_1 R_2} \Bigg\{ \delta_{l',l+1} C_{Jl}^{+} \Bigg[\delta_{n',n\pm1} C_{nl}^{+} \sqrt{\frac{(n_> + l + 1)(n_> - l - 1)}{(2n_> + 1)(2n_> - 1)}} \\
&- l\left(a_{n,l}\delta_{n',n+1} - b_{n,l}\delta_{n',n-1}\right) \Bigg] \\
&+ \delta_{l',l-1} C_{Jl}^{-} \Bigg[\delta_{n',n\pm1} C_{nl}^{-} \sqrt{\frac{(n_> - l + 1)(n_> + l - 1)}{(2n_> + 1)(2n_> - 1)}} \\
&+ l\left(a_{n,-l}\delta_{n',n+1} - b_{n,-l}\delta_{n',n-1}\right) \Bigg] \Bigg\},
\end{aligned} \tag{18}$$

with $a_{n,l} = \sqrt{(n + l + 1)(n + l + 2)/[(2n + 3)(2n + 1)]}$ and $b_{n,l} = \sqrt{(n - l - 1)(n - l)/[(2n - 1)(2n + 1)]}$.

The following expression results for the potential energy matrix elements:

$$\left\langle J\ l'\ n' \middle| \widehat{\mathrm{V}} \middle| J\ l\ n \right\rangle = \delta_{l',l} \sum_q C_q (-1)^l \sqrt{(2n+1)(2n'+1)} \times \begin{pmatrix} n' & q & n \\ 0 & 0 & 0 \end{pmatrix} \begin{pmatrix} n' & q & n \\ -l & 0 & l \end{pmatrix}, \tag{19}$$

where the matrices in brackets represent the Wigner 3-*j* symbol (see e.g. Ref. 104) and C_q are expansion coefficients of the bending potential in the basis of unnormalized Legendre polynomials:

$$V(\theta) = \sum_q C_q P_q(\cos\theta). \tag{20}$$

Diagonalization of the resulting matrix for a given value of angular momentum J then yields the energy levels $\epsilon_{J,i}$ and rigid-bender eigen-functions $\Psi_{J,i}^{\mathrm{rb}} = \sum_{l,n} d_i^{ln} |J\ l\ n\rangle$. The description up to this point did not consider the coupling of molecular rotation with electronic angular momentum. In the case of the $\tilde{\mathrm{X}}\ ^3\Sigma_g^-$ ground state, only coupling of rotation with spin is possible, leading to a

triplet splitting of each rovibrational level, except for states with $N = 0$. This splitting is small in general[89] and in the specific case of NCN[19] and was therefore neglected in our treatment. To be formally precise however, the total angular momentum quantum number J has to be replaced by the spinless quantum number N in the equations presented above.

In the case of the ã $^1\Delta_g$ state of NCN, which is characterized by an RT interaction, several modifications to the methodology have to be incorporated: as the electronic motion is no longer well separated from the nuclear motion, the rovibrational basis functions have to be multiplied by an electronic basis function. In analogy with the work of Perić et al.,[41] the following basis was chosen:

$$\Psi_{\mathrm{el}}^{+\Lambda} = \frac{1}{\sqrt{2}} \exp(i\Lambda\phi)\,(\Psi^+ + \Psi^-) \qquad (21)$$

$$\Psi_{\mathrm{el}}^{-\Lambda} = \frac{1}{\sqrt{2}} \exp(-i\Lambda\phi)\,(\Psi^+ - \Psi^-) \qquad (22)$$

Here, Λ is the azimuthal electronic quantum number ($\Lambda = 2$ for the Δ state), and $\Psi^{\pm}$ are the Born-Oppenheimer eigenstates of the electronic Schrödinger equation (corresponding to the upper and lower curves $1^1\mathrm{B}_1/1^1\mathrm{A}_1$ in Fig. 7): $\widehat{\mathrm{H}}_{\mathrm{el}}\Psi^+ = \mathrm{V}^+\Psi^+$ and $\widehat{\mathrm{H}}_{\mathrm{el}}\Psi^- = \mathrm{V}^-\Psi^-$. The electronic orbital angular momentum couples with the vibrational angular momentum to form the vibronic angular momentum $K = l \pm \Lambda$.

In addition, the potential energy operator $\widehat{\mathrm{V}}$ in Eq. (11) has to be replaced by the electronic Hamiltonian $\widehat{\mathrm{H}}_{\mathrm{el}}$. The matrix elements of $\widehat{\mathrm{H}}_{\mathrm{el}}$ in the electronic basis (Eqs. (21) and (22)) amount to:[41]

$$\left\langle \Psi_{\mathrm{el}}^{+\Lambda} \middle| \widehat{\mathrm{H}}_{\mathrm{el}} \middle| \Psi_{\mathrm{el}}^{+\Lambda} \right\rangle = \left\langle \Psi_{\mathrm{el}}^{-\Lambda} \middle| \widehat{H}_{\mathrm{el}} \middle| \Psi_{\mathrm{el}}^{-\Lambda} \right\rangle = \frac{1}{2}(V^+ + V^-) \qquad (23)$$

$$\left\langle \Psi_{\mathrm{el}}^{+\Lambda} \middle| \widehat{\mathrm{H}}_{\mathrm{el}} \middle| \Psi_{\mathrm{el}}^{-\Lambda} \right\rangle = \exp(-2i\Lambda\phi)\frac{1}{2}(V^+ - V^-) \qquad (24)$$

$$\left\langle \Psi_{\mathrm{el}}^{-\Lambda} \middle| \widehat{\mathrm{H}}_{\mathrm{el}} \middle| \Psi_{\mathrm{el}}^{+\Lambda} \right\rangle = \exp(2i\Lambda\phi)\frac{1}{2}(V^+ - V^-) \qquad (25)$$

Due to the exponential factors $\exp(\pm 2i\Lambda\phi)$ and the factor $\exp(il\phi)$ in the rovibrational basis (Eq. (14)), non-zero off-diagonal elements only arise for $l' = l - 2\Lambda$ (for $\Lambda' = +2,\ \Lambda = -2$) and $l' = l + 2\Lambda$ (for $\Lambda' = -2,\ \Lambda = +2$).

In the same way as the simple bending potential $V(\theta)$ in the non-RT case (Eq. (20)), the average potential and half difference potential in Eqs. (23) to (25) can be parameterized in terms of Legendre polynomials:

$$V_{\mathrm{avg}}(\theta) = \frac{1}{2}(V^{+}(\theta) + V^{-}(\theta)) = \sum_{q} C_q^{\mathrm{avg}} P_q(\cos\theta), \tag{26}$$

$$V_{\Delta/2}(\theta) = \frac{1}{2}(V^{+}(\theta) - V^{-}(\theta)) = \sum_{q} C_q^{\Delta/2} P_q(\cos\theta). \tag{27}$$

The rovibronic matrix elements of $\widehat{H}_{\mathrm{el}}$ are then evaluated according to Eq. (19), replacing the coefficients C_q by C_q^{avg} (for diagonal elements with respect to Λ) or $C_q^{\Delta/2}$ (off-diagonal elements w.r.t. Λ). In the latter case, $\delta_{l',l}$ has to be replaced by $\delta_{l',l-2\Lambda}$ or $\delta_{l',l+2\Lambda}$ (see selection rules above).

Furthermore, the matrix elements of the rovibrational kinetic energy operators have to be adapted due to the coupling between vibrational and electronic angular momentum. The operator $\widehat{\Pi}$ that is present in Eq. (13) corresponds to the total angular momentum operator. In principle, it must be replaced by $\widehat{\Pi} - \hat{\mathrm{L}}$, where $\hat{\mathrm{L}}$ is the electronic angular momentum operator. The dominant vibronic interaction occurs in the ${\widehat{\Pi}^2}_z$ part of the Hamiltonian,[101] thus only ${\widehat{\Pi}^2}_z$ was replaced by $\left(\widehat{\Pi}_z - \hat{\mathrm{L}}_z\right)^2$ in Eq. (13). Consequently, the following matrix elements for $\widehat{\mathrm{K}}_{\mathrm{vr}}$ result:

$$\begin{aligned}\left\langle J\ l'\ n'\ K'\ \Lambda' \middle| \widehat{\mathrm{K}}_{\mathrm{vr}}^{(1)} \middle| J\ l\ n\ K\ \Lambda \right\rangle \\ = \delta_{\Lambda',\Lambda} \frac{\hbar^2}{2\mu_1 R_1^2} \delta_{n',n} \{ \delta_{k',k}[J(J+1) - 2l^2] \\ - \delta_{k',k+1} C_{Jk}^{+} C_{nl}^{+} - \delta_{k\prime,k-1} C_{Jk}^{-} C_{nl}^{-} \}\end{aligned} \tag{28}$$

$$
\begin{aligned}
&\left\langle J\ l'\ n'\ K'\ \Lambda' \middle| \widehat{\mathrm{K}}_{\mathrm{vr}}^{(2)} \middle| J\ l\ n\ K\ \Lambda \right\rangle \\
&= \delta_{\Lambda',\Lambda} \frac{\hbar^2}{2\mu_{12} R_1 R_2} \Bigg\{ \delta_{K',K+1} C_{JK}^{+} \Bigg[\delta_{n',n\pm1} C_{nl}^{+} \sqrt{\frac{(n_> + l + 1)(n_> - l - 1)}{(2n_> + 1)(2n_> - 1)}} \\
&- K\left(a_{n,l}\delta_{n',n+1} - b_{n,l}\delta_{n',n-1}\right) \Bigg] \\
&+ \delta_{K',K-1} C_{JK}^{-} \Bigg[\delta_{n',n\pm1} C_{nl}^{-} \sqrt{\frac{(n_> - l + 1)(n_> + l - 1)}{(2n_> + 1)(2n_> - 1)}} \\
&+ K\left(a_{n,-l}\delta_{n',n+1} - b_{n,-l}\delta_{n',n-1}\right) \Bigg] \Bigg\}
\end{aligned}
\tag{29}
$$

The expressions for the $\widehat{\mathrm{K}}_{\mathrm{v}}$ part of the Hamiltonian (see Eqs. (15) and (16)) can be adopted without further modification if the restriction $\Lambda' = \Lambda$ is taken into account for these matrix elements.

References

[1] J. A. Miller, M. J. Pilling and J. Troe, Proc. Combust. Inst. **30**, 43 (2005).
[2] A. A. Konnov, Combust. Flame **156**, 2093 (2009).
[3] C. P. Fenimore, Proc. Combust. Inst. **13**, 373 (1971).
[4] J. A. Miller and S. P. Walch, Int. J. Chem. Kinet. **29**, 253 (1997).
[5] Q. Cui, K. Morokuma, J. M. Bowman and S. J. Klippenstein, J. Chem. Phys. **110**, 9469 (1999).
[6] L. V. Moskaleva and M. C. Lin, Proc. Combust. Inst. **28**, 2393 (2000).
[7] L. V. Moskaleva, W. S. Xia and M. C. Lin, Chem. Phys. Lett. **331**, 269 (2000).
[8] V. Vasudevan, R. K. Hanson, C. T. Bowman, D. M. Golden and D. F. Davidson, J. Phys. Chem. A **111**, 11818 (2007).
[9] L. B. Harding, S. J. Klippenstein and J. A. Miller, J. Phys. Chem. A **112**, 522 (2008).
[10] G. P. Smith, Chem. Phys. Lett. **367**, 541 (2003).
[11] J. A. Sutton, B. A. Williams and J. W. Fleming, Combust. Flame **153**, 465 (2008).
[12] R. E. Baren and J. F. Hershberger, J. Phys. Chem. A **106**, 11093 (2002).
[13] O. Welz and M. Olzmann, J. Phys. Chem. A **116**, 7293 (2012).
[14] A. Busch, N. González-García, G. Lendvay and M. Olzmann, J. Phys. Chem. A **119**, 7838 (2015).
[15] W.-S. Teng, L. V. Moskaleva, H.-L. Chen and M. C. Lin, J. Phys. Chem. A **117**, 5775 (2013).
[16] L. B. Harding, S. J. Klippenstein and A. W. Jasper, J. Phys. Chem. A **116**, 6967 (2012).
[17] J. Dammeier and G. Friedrichs, J. Phys. Chem. A **114**, 12963 (2010).
[18] K. R. Jennings and J. W. Linnett, Trans. Faraday Soc. **56**, 1737 (1960).
[19] G. Herzberg and D. N. Travis, Can. J. Phys. **42**, 1658 (1964).
[20] H. W. Kroto, J. Chem. Phys. **44**, 831 (1966).
[21] H. W. Kroto, Can. J. Phys. **45**, 1439 (1967).
[22] H. W. Kroto, T. F. Morgan and H. H. Sheena, Trans. Faraday Soc. **66**, 2237 (1970).
[23] S. A. Beaton, Y. Ito and J. M. Brown, J. Mol. Spectrosc. **178**, 99 (1996).
[24] S. A. Beaton and J. M. Brown, J. Mol. Spectrosc. **183**, 347 (1997).
[25] N. Lamoureux, C. M. Western, X. Mercier and P. Desgroux, Combust. Flame **160**, 755 (2013).
[26] D. E. Milligan, M. E. Jacox, J. J. Comeford and D. E. Mann, J. Chem. Phys. **43**, 756 (1965).
[27] D. E. Milligan and M. E. Jacox, J. Chem. Phys. **45**, 1387 (1966).
[28] D. McNaughton, G. F. Metha and R. Tay, Chem. Phys. **198**, 107 (1995).
[29] G. P. Smith, R. A. Copeland and D. R. Crosley, J. Chem. Phys. **91**, 1987 (1989).
[30] K. D. Hensel and J. M. Brown, J. Mol. Spectrosc. **180**, 170 (1996).
[31] M. Wienkoop, W. Urban and J. M. Brown, J. Mol. Spectrosc. **185**, 185 (1997).
[32] E. P. Clifford, P. G. Wenthold, W. C. Lineberger, G. A. Petersson and G. B. Ellison, J. Phys. Chem. A **101**, 4338 (1997).
[33] T. R. Taylor, R. T. Bise, K. R. Asmis and D. M. Neumark, Chem. Phys. Lett. **301**, 413 (1999).
[34] M. E. Jacox, J. Phys. Chem. Ref. Data **32**, 1 (2003).
[35] C. Thomson, J. Chem. Phys. **58**, 841 (1973).
[36] G. R. Williams, Chem. Phys. Lett. **25**, 602 (1974).
[37] C. W. Murray, G. J. Laming, N. C. Handy and R. D. Amos, J. Phys. Chem. **97**, 1868 (1993).
[38] J. M. L. Martin, P. R. Taylor, J. P. François and R. Gijbels, Chem. Phys. Lett. **226**, 475 (1994).
[39] H. U. Suter, M. B. Huang and B. Engels, J. Chem. Phys. **101**, 7686 (1994).
[40] M. Perić, M. Krmar, J. Radić-Perić and L. Stevanović, J. Mol. Spectrosc. **208**, 271 (2001).
[41] M. Perić, M. Krmar, J. Radić-Perić and M. Hanrath, J. Mol. Spectrosc. **204**, 226 (2000).

[42] P. Rajendra and P. Chandra, J. Chem. Phys. **114**, 1589 (2001).
[43] J. W. Ochterski, G. A. Petersson and J. A. Montgomery, J. Chem. Phys. **104**, 2598 (1996).
[44] S. Canneaux, A. Wallet, M. Ribaucour and F. Louis, Comp. Theor. Chem. **967**, 67 (2011).
[45] L. A. Curtiss, P. C. Redfern and K. Raghavachari, J. Chem. Phys. **126**, 084108 (2007).
[46] D. E. Milligan, M. E. Jacox and A. M. Bass, J. Chem. Phys. **43**, 3149 (1965).
[47] C.-G. Ci, X.-M. Duan, J.-Y. Liu and C.-C. Sun, Acta Phys. Chim. Sin. **26**, 2787 (2010).
[48] F. D. Marsh and M. E. Hermes, J. Am. Chem. Soc. **87**, 1819 (1965).
[49] D. J. Benard, C. Linnen, A. Harker, H. H. Michels, J. B. Addison and R. Ondercin, J. Phys. Chem. B **102**, 6010 (1998).
[50] A. Busch and M. Olzmann, Proceedings of the European Combustion Meeting, Vienna, Austria, April 14-17 2009, pp. 810138.
[51] J. Dammeier, B. Oden and G. Friedrichs, Int. J. Chem. Kinet. **45**, 30 (2013).
[52] J. Hetzler and M. Olzmann, Z. Phys. Chem. **229**, 1503 (2015).
[53] R. N. Schwartz, Z. I. Slawsky and K. F. Herzfeld, J. Chem. Phys. **20**, 1591 (1952).
[54] R. N. Schwartz and K. F. Herzfeld, J. Chem. Phys. **22**, 767 (1954).
[55] MOLPRO, version 2012.1, a package of ab initio programs, H.-J. Werner, P. J. Knowles, G. Knizia, F. R. M. and, M. Schütz, P. Celani, T. Korona, R. Lindh, A. Mitrushenkov, G. Rauhut, K. R. Shamasundar, T. B. Adler, R. D. Amos, A. Bernhardsson, A. Berning, D. L. Cooper, M. J. O. Deegan, A. J. Dobbyn, F. Eckert, E. Goll, C. Hampel, A. Hesselmann, G. Hetzer, T. Hrenar, G. Jansen, C. Köppl, Y. Liu, A. W. Lloyd, R. A. Mata, A. J. May, S. J. McNicholas, W. Meyer, M. E. Mura, A. Nicklass, D. P. O'Neill, P. Palmieri, D. Peng, K. Pflüger, R. Pitzer, M. Reiher, T. Shiozaki, H. Stoll, A. J. Stone, R. Tarroni, T. Thorsteinsson and M. Wang, 2012, Cardiff, UK.
[56] Y. J. Bomble, J. F. Stanton, M. Kállay and J. Gauss, J. Chem. Phys. **123**, 054101 (2005).
[57] MRCC, a quantum chemical program suite, www.mrcc.hu, M. Kállay, Z. Rolik, I. Ladjánszki, L. Szegedy, B. Ladóczki, J. Csontos and B. Kornis, 2013, Budapest, Hungary.
[58] Z. Rolik, L. Szegedy, I. Ladjánszki, B. Ladóczki and M. Kállay, J. Chem. Phys. **139**, 094105 (2013).
[59] T. H. Dunning, J. Chem. Phys. **90**, 1007 (1989).
[60] T. B. Adler, G. Knizia and H.-J. Werner, J. Chem. Phys. **127**, 221106 (2007).
[61] H. J. Werner and P. J. Knowles, J. Chem. Phys. **89**, 5803 (1988).
[62] P. J. Knowles and H.-J. Werner, Chem. Phys. Lett. **145**, 514 (1988).
[63] P. J. Knowles and H.-J. Werner, Theor. Chim. Acta **84**, 95 (1992).
[64] S. R. Langhoff and E. R. Davidson, Int. J. Quantum Chem. **8**, 61 (1974).
[65] H.-J. Werner, Mol. Phys. **89**, 645 (1996).
[66] P. Celani and H.-J. Werner, J. Chem. Phys. **112**, 5546 (2000).
[67] F. Weigend and R. Ahlrichs, Phys. Chem. Chem. Phys. **7**, 3297 (2005).
[68] B. Ruscic, R. E. Pinzon, G. v. Laszewski, D. Kodeboyina, A. Burcat, D. Leahy, D. Montoy and A. F. Wagner, J. Phys. Conf. Ser. **16**, 561 (2005).
[69] Active Thermochemical Tables (ATcT) values based on ver. 1.118 of the Thermochemical Network, B. Ruscic, http://ATcT.anl.gov, 2015.
[70] S. Baumgärtel, K. H. Gericke and F. J. Comes, Ber. Bunsenges. Phys. Chem. **98**, 1009 (1994).
[71] H. Okabe and A. Mele, J. Chem. Phys. **51**, 2100 (1969).
[72] NST: A simple minimum-on-the-seam-of-crossings (MSX) optimizer and nonadiabatic statistical theory (NST) flux calculator, http://tcg.cse.anl.gov/papr/codes/nst.html, A. Jasper, 2016, Sandia and Argonne National Laboratories.

[73] J. C. Lorquet and B. Leyh-Nihant, J. Phys. Chem. **92**, 4778 (1988).
[74] J. N. Harvey, Phys. Chem. Chem. Phys. **9**, 331 (2007).
[75] A. W. Jasper, J. Phys. Chem. A **119**, 7339 (2015).
[76] A. O. Lykhin, D. S. Kaliakin, G. E. dePolo, A. A. Kuzubov and S. A. Varganov, Int. J. Quantum Chem. **116**, 750 (2016).
[77] J. B. Delos and W. R. Thorson, Phys. Rev. A **6**, 728 (1972).
[78] W. Forst, *Unimolecular Reactions: A Concise Introduction* (Cambridge University Press, Cambridge, UK, 2003).
[79] N. Koga and K. Morokuma, Chem. Phys. Lett. **119**, 371 (1985).
[80] U. Bley and F. Temps, J. Chem. Phys. **98**, 1058 (1993).
[81] A. Bondi, J. Phys. Chem. **68**, 441 (1964).
[82] W. M. Gelbart and K. F. Freed, Chem. Phys. Lett. **18**, 470 (1973).
[83] K. F. Freed, Adv. Chem. Phys. **47**, 291 (1981).
[84] K. F. Freed, Adv. Chem. Phys. **42**, 207 (1980).
[85] G. Herzberg and E. Teller, Z. Phys. Chem. **B21**, 410 (1933).
[86] U. Bley, M. Koch, F. Temps and H. G. Wagner, Ber. Bunsenges. Phys. Chem. **93**, 833 (1989).
[87] K. L. Gannon, M. A. Blitz, T. Kovács, M. J. Pilling and P. W. Seakins, J. Chem. Phys. **132**, 024302 (2010).
[88] D. S. McClure, J. Chem. Phys. **17**, 665 (1949).
[89] G. Herzberg, *Molecular Spectra and Molecular Structure III. Electronic Spectra and Electronic Structure of Polyatomic Molecules* (Van Nostrand, Princeton, NJ, 1966).
[90] A. R. W. McKellar, P. R. Bunker, T. J. Sears, K. M. Evenson, R. J. Saykally and S. R. Langhoff, J. Chem. Phys. **79**, 5251 (1983).
[91] I. I. Guseinov, B. A. Mamedov and A. S. Ekenoğlu, Z. Naturforsch. A **61**, 141 (2006).
[92] P. R. Bunker and J. M. R. Stone, J. Mol. Spectrosc. **41**, 310 (1972).
[93] H. A. Mavromatis and R. S. Alassar, Appl. Math. Lett. **12**, 101 (1999).
[94] S.-H. Dong and R. Lemus, Appl. Math. Lett. **15**, 541 (2002).
[95] C. G. Stevens and J. C. D. Brand, J. Chem. Phys. **58**, 3324 (1973).
[96] J. N. Harvey, M. Aschi, H. Schwarz and W. Koch, Theor. Chem. Acc. **99**, 95 (1998).
[97] T. Stoecklin, O. Denis-Alpizar, P. Halvick and M.-L. Dubernet, J. Chem. Phys. **139**, 124317 (2013).
[98] S. Carter and N. C. Handy, Mol. Phys. **47**, 1445 (1982).
[99] B. T. Sutcliffe and J. Tennyson, Mol. Phys. **58**, 1053 (1986).
[100] B. T. Sutcliffe, Mol. Phys. **48**, 561 (1983).
[101] S. Carter and N. C. Handy, Mol. Phys. **52**, 1367 (1984).
[102] D. A. Varshalovich, A. N. Moskalev and V. K. Khersonskii, *Quantum theory of angular momentum* (World Scientific, Singapore, 1986).
[103] T. Stoecklin, Personal Communication, 09/08/2016.
[104] D. M. Brink and G. R. Satchler, *Angular Momentum* (Clarendon Press, Oxford, 1962).